Fabrication and Characterization of Flexible and Implantable Medical Devices for Optogenetics and Neural Signal Recording

by

Jeongpil Park

A dissertation submitted in partial fulfillment of

the requirements for the degree of

Doctor of Philosophy

(Electrical and Computer Engineering)

at the

UNIVERSITY OF WISCONSIN-MADISON

2021

Date of final oral examination: 01/11/2021

The dissertation is approved by the following members of the Final Oral Committee:

Zhenqiang Ma, Professor, Electrical and Computer Engineering

Justin C. Williams, Professor, Biomedical Engineering

Zongfu Yu, Associate Professor, Electrical and Computer Engineering

Chu Ma, Assistant Professor, Electrical and Computer Engineering

© Copyright by Jeongpil Park 2021

All Rights Reserved

To my family

ACKNOWLEDGEMENT

My research achievements would not have been possible without the support and encouragement from my family, my advisor, colleagues, and friends at the University of Wisconsin-Madison. I would like to firstly express my deepest gratitude to my advisor, Prof. Zhenqiang (Jack) Ma, for his guidance, constant inspiration and supports. Diligence and concentration are the most valuable that I learned from Prof. Ma and it helps me to make my future career path. In the same spirit, I wish to extend my utmost appreciation to Prof. Justin Williams for his sincere supervision and support. I think myself very lucky to have completed my work under his guidance. I would also like to thank Prof. Zongfu Yu and Prof. Chu Ma for their valuable comments and generous help as my committee members.

Moreover, I would like to express my gratitude to current and former Ma group members: Dr. Tong June Kim, Dr. Munho Kim, Dr. Jaeseong Lee, Dr. Sang June Cho, Dr. Dong Liu, Dr. Cuong Manh Nguyen, Dr. Jung Hun Seo, Dr. Solomon Mikael, Dr. Dong-Wook Park, Dr. Kwangeun Kim, Dr. Yei Hwan Jung, Dr. Juhwan Lee, Dr. Jihye Bong, Dr. Tzu-Hsuan Chang, Dr. Zhenyang Xia, Dr. Huilong Zhang, Dr. First Yassar, Jisoo Kim, Inkyu Lee, Jiarui Gong, Shuoyang Qui, Wei Lin, Seunghwan Min, Jie Zhou, Yu Lan, and Hokyung Jang. I especially thank Dr. Tong June Kim, Dr. Soongyu Yi, and Jisoo Kim for being on the journey together. It was less burden and pleasant during my Ph. D. study with you. Also, I am grateful for my collaborator Professor Justin Williams group members: Dr. Aaron Suminski, Dr. Kevin Cheng, Sarah Brodnick, Stephan Blanz, Jack Kegel, and Jared P. Ness. They gave me a constructive feedback about my research.

I also would like to express my gratitude to my dear friends: Dr. Kyunghee Kim, Dr. Wooyoung Choi, Dr. Hyeonjun Lee, Dr. Donghoon Lee, and Jae Ha Ryu.

I am very thankful for the funding agencies/programs: Department of Defense (DOD),

Defense Advanced Research Projects Agency (DARPA, Reference number: N66001-17-2-4010); DOD, Army (Reference number: W911NF-14-1-0652); DOD, Navy (Reference number: N00014-13-1-0226); DOD, Air force (Reference number: FA9500-09-01-0482); DOD, DARPA (Reference number: RC104707-UW), collaborated with Michigan State University (MSU); Department of Energy (DOE), National Nuclear Security Administration (Reference number: DE-NA0002915); U.S. Endowment for Forestry and Communities (Reference number: E17-21); National Institute of Health (NIH, Reference number: 1R01NS101013-01A1); Foundation Fighting Blindness (Reference number: TA-RM-1016-0700-UW-GH); National Science Foundation (NSF, Reference number: DMR-1124131/0024232 (011288-2)), collaborated with University of Pittsburgh; Wisconsin Alumni Research Foundation (WARF, Reference or Project number: AAA4178, AAA4884, AAA8632).

I would like to thank Daniel Christensen, Quinn Leonard, Hal Gilles, Kurt Kupcho, and other NFC (former WCAM) cleanroom facility staffs for their dedications on the maintenance of the cleanroom, the equipment, and the training provided to users.

I am grateful for the continued support and love of my family. My father Seonhwan Park, my mother Eunsook Kim, and my sister Yeonju Park have stood by me since the beginning.

Finally, I want to thank my dearest loving fiancé Nari Kim. It was her encouragement, support, and joyful smile that kept me going for completing my degree.

ABSTRACTS

This thesis systematically studies two main topics, namely, a design and fabrication of a combined device between optoelectronics and transparent graphene-based electrodes and a development of an implantable micro-electrocorticography for a chronic implantation.

The first topic introduces the design and fabrication of the flexible and implantable combined device for optogenetics area. The optoelectronics is utilized the commercial blue LED component to stimulate Channelrhodopsin-2 (ChR2) mouse model, which is a blue light-gated non-specific cation channel that neuronal activation. The micro-electrocorticography device is used the transparent graphene-based electrodes instead of the metal electrodes for recording a neural signal. Graphene that is a novel material consisting of carbon atoms, has a broad wavelength transparency from ultraviolet (UV) to infrared (IR) range. Moreover, graphene has superior properties such as electrical conductivity, mechanical flexibility, and biocompatibility etc. These advantages of graphene make it a promising material for the next generation biomedical application. Finally, we demonstrate a fully implantable system utilizing microscale LEDs vertically stacked on top of transparent graphene-based electrodes which the light can pass through, enabling synchronous a light stimulation and a neural signal recording.

The second topic is on the implantable micro-electrocorticography for a chronic implantation using a 3D-printed cranial prothesis. It also allows the internal neural signal recording of the dorsal cerebral cortex of the rodent model. The photocurable polyimide (PI) substrate allows the stable mechanical property of the fabricated device. Compared to fMRI and MEG application areas, our device has a good spatial and temporal resolution. We also demonstrated the implantation method using the fabricated device and figure out the improvement in the next batch experiment. They have a potential to apply and impact the internal neural signal recording area and the neural image research field in the future.

TABLE OF CONTENTS

LIST OF FIGURES

LIST OF EQUATIONS

CHAPTER 1. Introduction

1.1. Optogenetics

In 2006, the term of optogenetics was firstly introduced by Deisseroth et al. [1] and it is an innovative biological technology to control the activity of cells using genetic engineering and optical technology. It is a useful and popular method to understand the nervous system in neuroscience research due to its spatial and temporal accuracy [2].

The nerve system can be broadly categorized into two major area: central nervous system (CNS) and peripheral nervous system (PNS) [3]. The CNS consists of two parts: the brain and the spinal cord [3]. The PNS includes the nerves and ganglia outside of the brain and spinal cord [3].

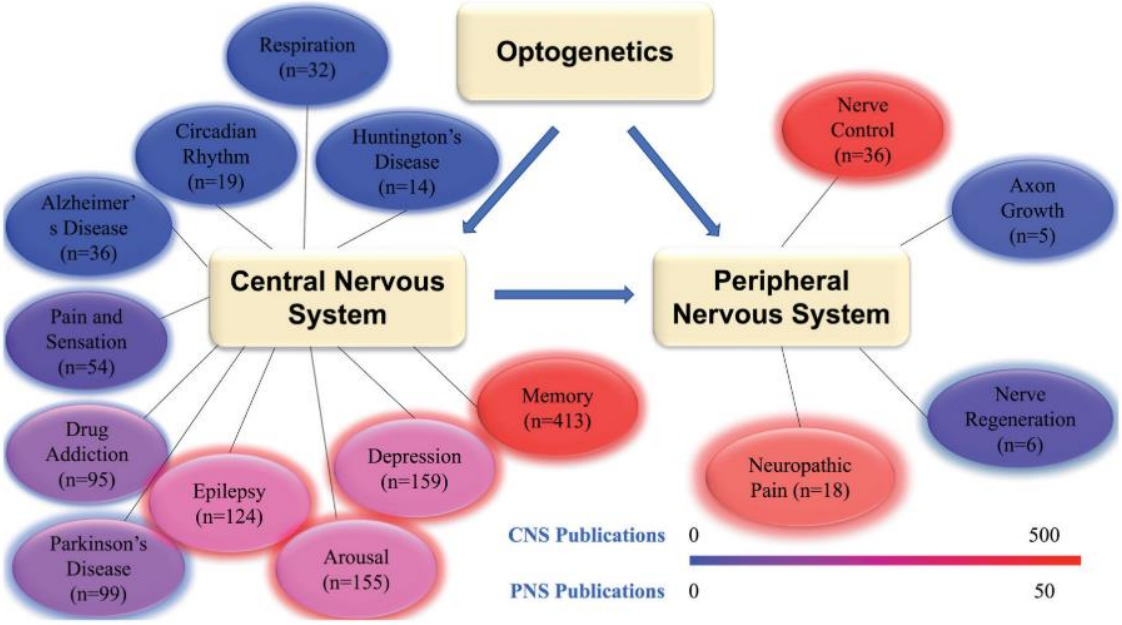

Figure 1.1. A visual diagram of the distribution between the CNS and the PNS based on different optogenetic applications [4]. (n: number of publications)

Since 2015, the latest applications in neuroscience using optogenetic applications from the CNS to the PNS are counted in the variety of neural regeneration (Figure 1.1) [4]. The many optogenetic applications play a major and leading role in the nerve system.

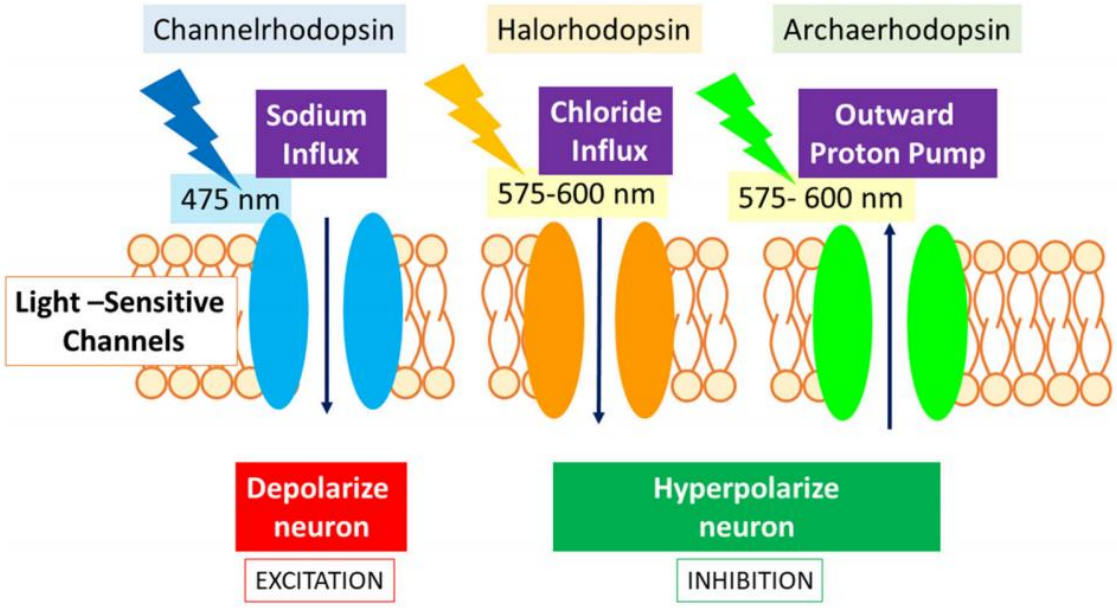

Figure 1.2. Common opsins in optogenetics. Channelrhodopsin (ChR) opens upon excitation with blue light (475 nm) and permit a cation influx into the cell when stimulated that depolarized the neuron. Halorhodopsin (NpHR) and archaerhodopsin (Arch) silence the neuron by hyperpolarization (inhibition) when they open the light-sensitive channels with yellow and yellow-green lights, respectively (575-600 nm). Upon light stimulation, NpHR allows chloride influx and Arch pumps protons out of the cell, respectively [2].

Generally, optogenetic actuators are proteins that modify the cell activity when they are expressed in response to illumination. The most common and used actuators are opsins. It can be categorized into two parts: microbial opsins (Type I) and vertebrate opsins (Type II) [5,6]. Type I opsins were used in the first optogenetics experiments because of genetic engineering using a single component protein and their faster kinetics compared to Type II opsins. The common microbial opsins are shown in Figure 1.2. The microbial opsins can be divided into two types: depolarizing (excitation) microbial opsins (channelrhodopsins) and hyperpolarizing (inhibition) microbial opsins (halorhodopsins and archaerhodopsin) [2,4–6]. Channelrhodopsin (ChR) opens upon excitation with blue light (475 nm) and permit a cation influx into the cell when stimulated that depolarized the neuron. Halorhodopsin (NpHR) and

archaerhodopsin (Arch) silence the neuron by hyperpolarization (inhibition) when they open the light-sensitive channels with yellow and yellow-green lights, respectively (575-600 nm). Upon light stimulation, NpHR allows chloride influx and Arch pumps protons out of the cell, respectively [2,5].

Both microbial opsins and vertebrate rhodopsins share architectural similarities and are consisted of seven transmembrane (TM) α-helices, called opsins and a photosensitive chromophore, called retinal [7]. Upon illumination at a targeted and specific wavelength, retinal in microbial rhodopsin is going to start an isomerization from all-trans to 13-cis that initiates a series of photocycle (Figure 1.3.) [8]. For vertebrate opsins, they undergo an isomerization from 11-cis to all-trans. This reaction makes the generation of unique photo-intermediates that lead to change of proteins that caused a channel opening, closing, and ionic conductance of the rhodopsin [9,10].

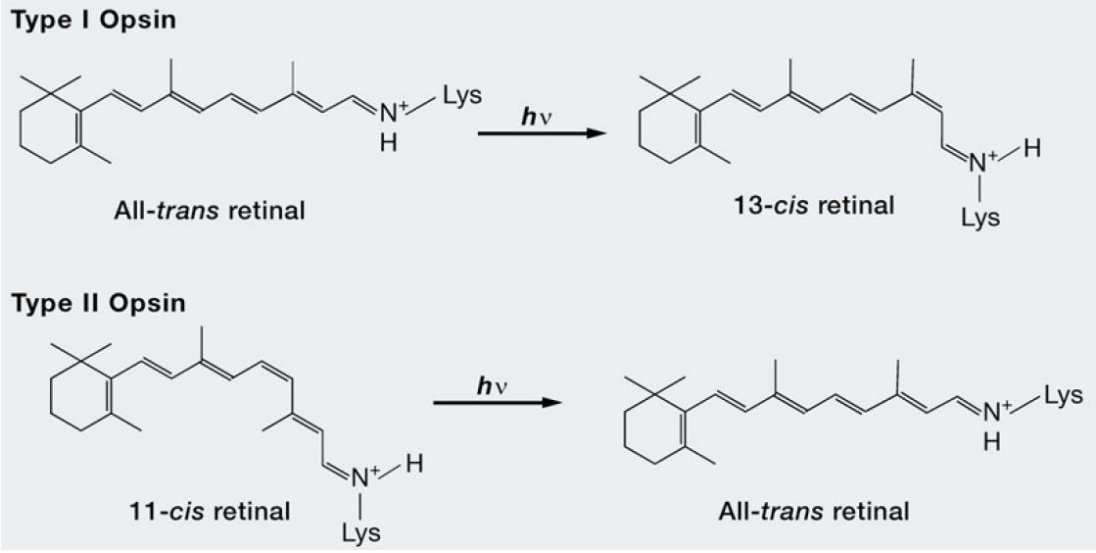

Figure 1.3. Photoreaction mechanism. Light-mediated isomerization of the retinal Schiff base (RSB). Top: Type I Opsin. Bottom: Type II opsin [8].

Using Optogenetics in the field of neuroscience, it has a chance to changing the neuroscience area. We can proceed a new generation of experiments to explore the roles of specific neural circuit components in normal and dysfunctional behavior [5].

1.2. Micro-Electrocorticography (µECoG)

In the recording system for multichannel neural interfaces, the methods of interfacing with the cerebral cortex and recording electrodes can be categorized into four parts: electroencephalography (EEG) for external scalp recordings, electrocorticography (ECoG) and micro-electrocoticography (µECoG) for surface cortical recordings, and penetrating electrode arrays for intracotical recordings in the brain [11]. These device types have their advantages and disadvantages in terms of invasiveness and spatial resolution (Figure 1.4.) [11].

Compared to ECoG electrode arrays, µECoG electrode arrays have micro-scale size diameters of electrodes for recording the neural signal (Figure 1.4.a-b). It means that µECoG device has a more spatial resolution compared to the conventional ECoG devices that are used the approximately 1 cm diameter of the recording electrode sites. Among these four types, µECoG electrode arrays provide a promising system due to neural signal acquisition, spatial resolution, and a less invasiveness properties (Figure 1.4.c).

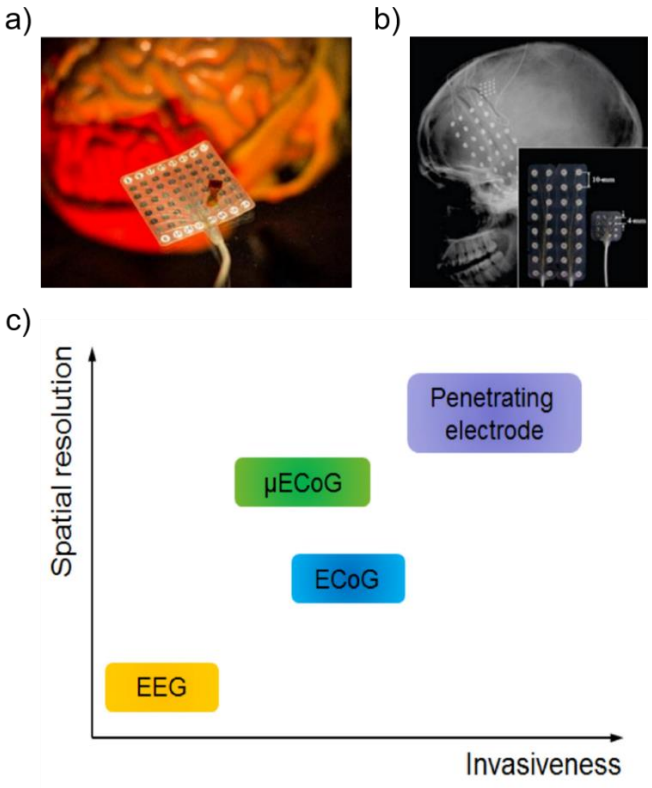

Figure 1.4. a) Photograph of comparison between ECoG and μECoG array [11]. b) X-ray image showing the implanted conventional ECoG and μECoG electrodes [12]. c) The graph with respect to spatial resolution and invasiveness for four types of neural electrodes [11].

CHAPTER 2. Design and Fabrication of Combined Device between Optoelectronics and Transparent Graphene-based Electrodes for Light Stimulation and Neural Signal Recording

2.1. Introduction

Flexible electronics which can be bent, folded and/or stretched, have potential used in various applications, such as biomedical implantation and wearable devices, due to their structure to facilitate less invasive clinical operation [13–17]. Flexible devices combined with optoelectronic systems extend to a range of applications such as biomedical stimulations and recordings using light sources, especially as optogenetics [18,19]. Optogenetics is a powerful technique involving a genetic modification of neural cells to make them reaction to a specific light stimulation by a selective excitation or inhibition of targeted neuron types for neural interfacing devices [20]. To utilize this method, it is necessary to deliver a specific light into the cortex for the direct stimulation.

Neural surface electrode arrays, such as micro-electrocorticography (μECoG) devices, provide a promising system according to neural signal acquisition, spatial resolution, a proper invasiveness [21–24]. However, these devices normally use opaque metallic conductive materials. Recently, many research studies have shown that graphene is an excellent candidate as a recording electrode due to its excellent electrical/thermal conductivity, transferability, and mechanical properties [25–29]. Furthermore, the biocompatibility and broad-wavelength transparency from the ultraviolet (UV) to the infrared radiation (IR) spectrum of graphene make it ideal for the replacement of metal counterparts in optogenetics stimulations, recordings, and imaging applications [30]. Because light is the primary stimulation tool for optogenetics, optoelectronics benefit from using transparent devices by precisely matched exposing light on the recording site through transparent electrodes. To deliver light into the cortex at the targeted

brain areas, the conventional method is used the optical fiber as the light source for a neural stimulation, externally [26,31,32]. However, the light sources have low spatial resolution due to the number of beams and the relatively imprecise positioning between a stimulation and recording area. To solve this problem, commercial micro light emitting diode (μLED) arrays [33–35], optical waveguide arrays [36,37], a fabricated passive Si photodiode array [38], and high-density μLED array [39] have been applied for the precise individual addressing. Moreover, recording devices with an internally mounted light source are capable of the operating under fully implanted condition.

According to Ji et al., commercial μLEDs have been fabricated on their polyimide-based (yellow-color) μECoG device by a wire bonding method and conductive silver paste for a good metal connection on the Au pads/polyimide (PI) [33,34]. However, not only transparent conductive materials but also clear (or transparent) substrate are important material characteristics for optoelectronics. Also, delicate fabrication technique of metal connection should be considered in sequence without the additional fabrication process in the same batch. Meanwhile, a transparent, flexible, and biocompatible Parylene C substrate was used to directly fabricate a monolithic device design in which GaN μLED and recording electrodes [40]. This design has 25 μm gap between recording electrode and μLED. However, it requires the same position to get the exact neural signal at the precise same area between the stimulation and recording area.

In this work, we demonstrate a fully implantable system utilizing microscale LEDs vertically stacked on top of transparent graphene-based electrodes which the light can pass through, enabling synchronous a light stimulation and a neural signal recording for neural interfacing.

2.2. Design of Optoelectronic and Transparent µECoG devices

We developed a unique design of optoelectrical neural stimulation and transparent µECoG devices. The design purpose is the combination of integrated optoelectronics and distributed transparent nerve signal recording electrodes on the flexible substrate for detecting the optical evoked potential. The simultaneous stimulating and recording in one device are aimed to Channelrhodopsin-2 (ChR2) mouse model, which is a blue light-gated non-specific cation channel that neuronal activation [41].

Figure 2.1.a schematically shows the device structure both the integrated blue µLED (dominant 456.5 nm wavelength) and transparent graphene-based µECoG devices which are on flexible polymer substrates. The flexible substrate materials are Noland Optical Adhesive 61 (NOA 61, NORLAND Products), SU-8, and polyethylene terephthalate (PET). Also, 4 × 4 µLED arrays for the optical stimulation is matched the location of 4 × 4 graphene channels for the neural signal recording, as shown in Figure 2.1.a and Figure 2.2.

The dimension considered to fit into the mouse brain size. The dimensions (width W, and length L) of the area of the integrated µLED and transparent graphene-based µECoG electrodes arrays are approximately 2.13 × 1.89 mm^2 (Figure 2.2.a) and 1.87 × 1.96 mm^2 (Figure 2.2.b), respectively. The detailed dimension information is written as follows; Commercial µLED chip (C460TR2227-0333, Cree Inc., USA) is 220 (W) × 270 (L) $µm^2$ and diameter of the graphene electrode is 150 µm. The center to center spacing or pitch between the two neighboring µLED and the two adjacent graphene-based electrode sites is designed as 500 µm. The fabricated combined device is shown in Figure 2.1.b after the attachment process.

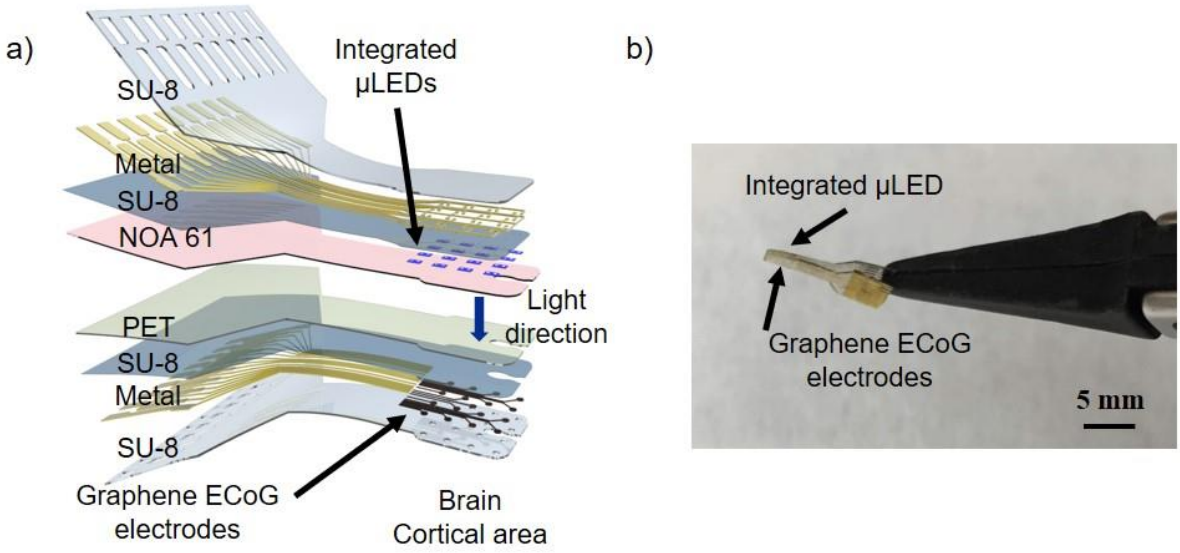

Figure 2.1. Schematic illustration and optical image of the combined device. a) the integrated blue μLEDs, NOA 61 (50 μm)/μLEDs (50 μm)/SU-8 (400 nm)/Metal electrode (Cr 10 nm/Au 350 nm)/SU-8 (1.5 μm) and graphene-based μECoG devices, PET (100 μm)/SU-8 (3 μm)/Metal electrode (Ti 50 nm/Au 200 nm)/four-layered graphene electrodes (1.2 nm)/SU-8 (10 μm) for optical stimulation and neural signal recording, respectively. b) A combined corresponding device both the integrated blue μLEDs and graphene-based ECoG devices.

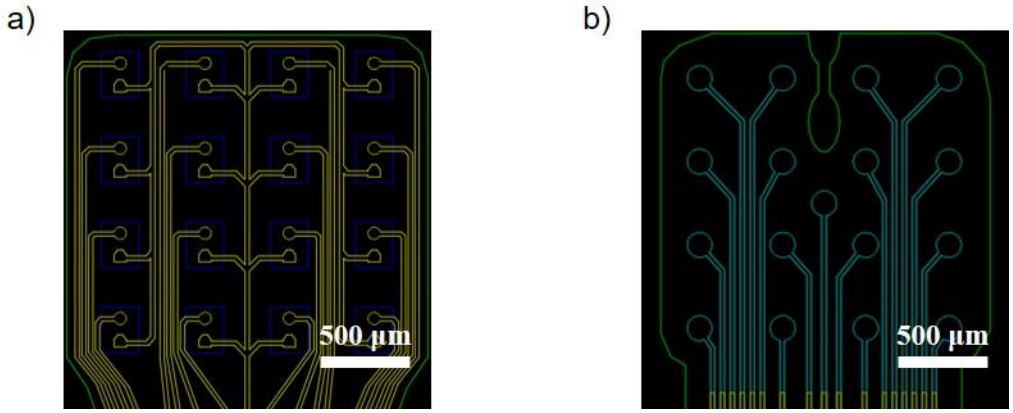

Figure 2.2. Schematic of the device design, a) flexible integrated μLEDs for optoelectrical neural stimulation and b) transparent graphene-based μECoG devices. (green line: outline of substrate, dark blue line: the shape of μLED, light blue line: graphene electrode, yellow line: metal electrode)

2.3. Fabrication of µLEDs array device

The integrated µLEDs array fabrication process can be divided into two steps. The first step is the preparation of the transferred 16 µLEDs on handling substrate. The second step is the integration process for optoelectronic. The detailed fabrication processes are shown in Figure 2.3. and Figure 2.4.

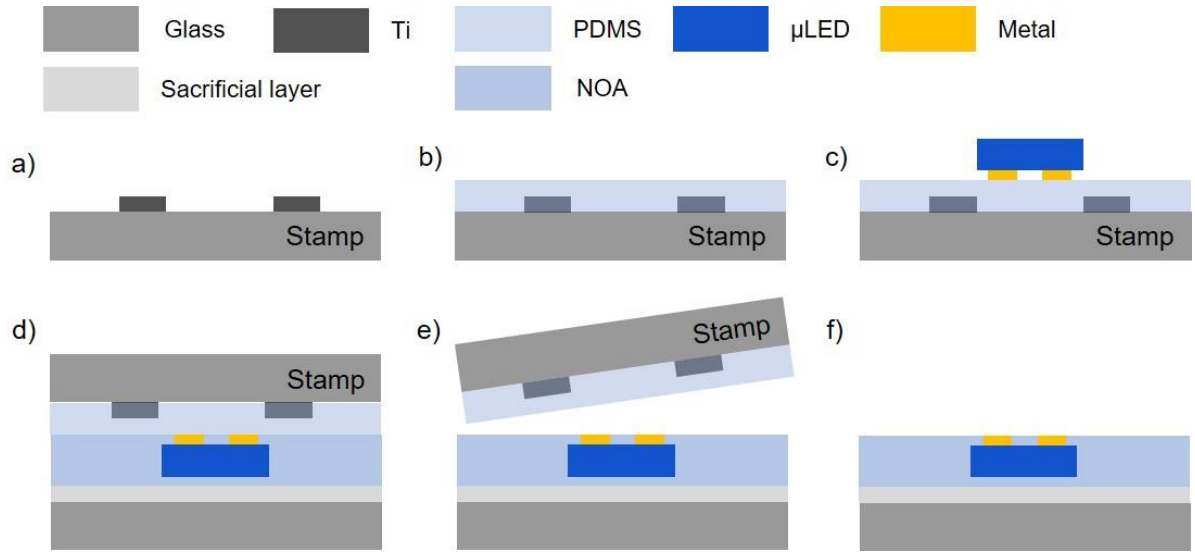

Figure 2.3. Schematic illustration of µLEDs transfer process using a stamp method. a) Metal deposition (Ti, 30 nm) as an align mark for transfer process on a precleaned glass substrate. b) Coat and bake PDMS (15:1) layer to stick µLED on the top surface. c) Transfer µLED on PDMS layer and d) attach a stamp substrate with handling substrate which is deposited a sacrificial layer (Ti/Pt/Ti/Al) using NOA material. After curing process by UV light for 90 mins, e) detach the stamp substrate and remain the LEDs on the handling substrate, f) Embedded µLED on a polymer layer/precleaned glass substrate.

First, as shown in Figure 2.3., the fabrication process begins with preparing a glass slide (Fisher Scientific, 25 × 75 × 1 mm^3) as a stamp substrate that was cleaned by ultrasonication with acetone, isopropyl alcohol (IPA), and deionized water (AQUA

SOLUTIONS, resistance: 18 MΩ) and dried at 110 °C for 1 min on a hot plate prior to use. The photoresist (PR) layer on a cleaned glass slide is prepared by spin-coating an image reversal PR (AZ 5214E, MICRO CHEM, 2,500 rpm, 30 sec) and soft-baking at 95 °C for 3 mins. In Figure 2.3.a, the aligned marks to transfer μLED arrays were generated through contact-mode lithography using a mask aligner (MJB3, KARL SUSS, illumination: 5.5 mW/cm^2, 2.3 sec), hard-baking at 115 °C for 90 secs, exposed sufficient ultraviolet lights for flood exposure for 25 secs at the same illumination intensity. The next step is developing the image reversal photoresist with a developer (AZ 917, MICRO CHEM) for 30 secs. Titanium (Ti, 30 nm) layer is deposited in sequence by an e-beam evaporator (Vacuum deposition system, ANGSTROM ENINEERING, 2×10^{-6} Torr). After finishing lift-off process with acetone, polydimethylsiloxane (PDMS, SYLGARD 184 Silicon elastomer base and curing agent, DOW CORNING, ratio: 15:1) layer is covered them by spin-coating (4000 rpm, 60 sec, ramp up condition) and baked at 120 °C for 60 mins (Figure 2.3.b). Figure 2.3.c shows that μLED is transferred on the stamp substrate within the aligned mark.

The device fabrication using an ultrathin polymer film as a substrate is difficult because of the lack of rigidity. To support a stable further fabrication, it is desirable to use an additional handling substrate [17]. The handling substrate is prepared a glass slide (Fisher Scientific, $75 \times 50 \times 1.2$ mm^3) that was cleaned by the same method. The metal layers, Ti (15 nm)/Platinum (Pt, 100 nm)/Ti (15 nm)/Aluminum (Al, 200 nm), are deposited as a sacrificial layer in sequence by an e-beam. Figure 2.3.d shows that second transfer process which the sixteen μLEDs array moves from the stamp substrate to a handling substrate. The NOA 61 is used to planarize for matching a same thickness, then is cured by exposing to UV light for 90 mins. Finally, the stamp substrate is detached from a handling substrate (Figure 2.3.e) and remain sixteen μLEDs array on a handling substrate on the proper position for a further process (Figure 2.3.f or Figure 2.4.a).

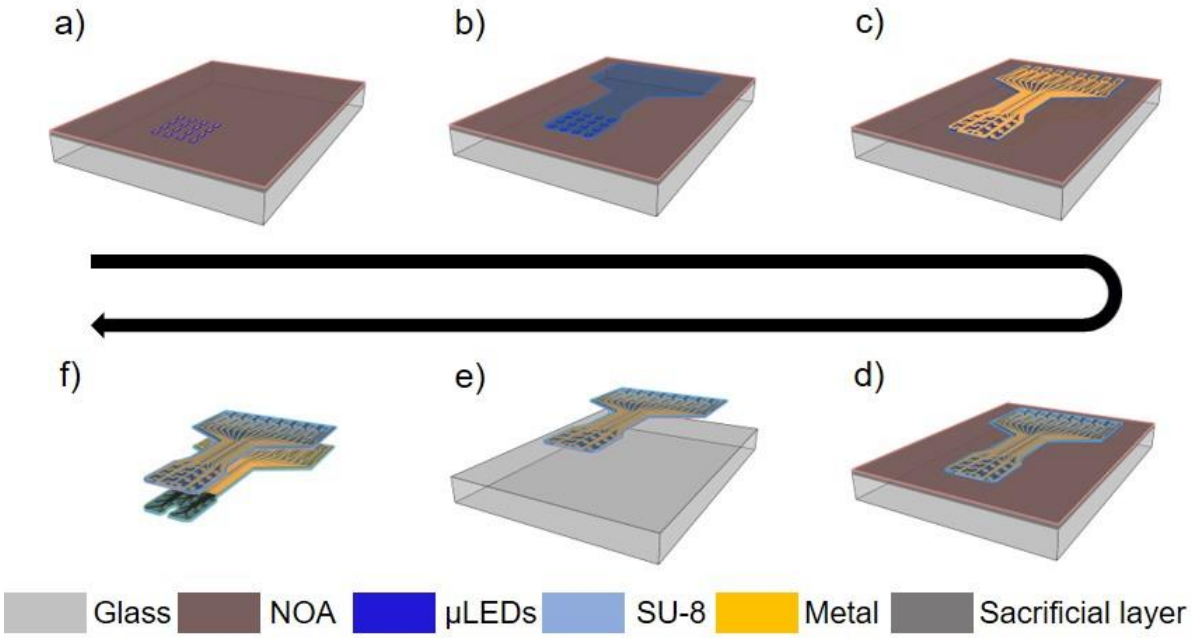

Figure 2.4. Schematic illustration of the fabrication process for optoelectronic device. a) Embedded μLEDs array on polymer layer/Glass substrate. b) Coated and etched SU-8 layer and c) Deposited the metal electrodes by e-beam evaporator and life-off process. d) Defined the passivation layer, SU-8, on the device and e) released the fabricated devices on the handling substrate by anodic metal dissolution method. f) Attached the backside of both the integrated μLEDs and the graphene-based μECoG devices.

A detailed fabrication process of 4 × 4 micro blue LED arrays for an optical stimulation is shown in Figure 2.4. The embedded μLEDs array on polymer layer (Figure 2.4.a) are passivated to define and protect the μLED electrode areas by coating SU-8 layer on the top surface in Figure 2.4.b. SU-8 negative PR (2000.5, MICRO CHEM, 3000 rpm for 30 sec, ramp up condition) is spin-coated on the μLEDs array sequentially and soft-baked at 95 °C for 1 min. To get a thicker passivation layer, same coating and baking process are processed once again. The passivation layer is cured by exposed UV light for 10 mins and hard-baked from 65 °C to 150 °C for 1 min and 5 mins, respectively. During a hard baking process, it needs to warm up slowly and cool down slowly to room temperature avoiding the crack of SU-8 layer due to the

difference of thermal expansion coefficient between SU-8 and NOA 61 layers on a handling substrate. Oxygen plasma treatment (Reactive ion etching, RIE, 10NR, SAMCO, O_2 40 sccm, 120 mTorr, 40 W, 30 sec) is processed to clean a top surface and to make hydrophilic surface for a next fabrication process. To make a copper (Cu) layer as an etching block layer, a positive PR (S1813, MICRO CHEM, 2500 rpm, 30 sec) is coated and baking at 105 °C for 3 mins. The pattern is generated through contact-mode lithography using MJB3 mask aligner (illumination: 5.5 mW/cm^2, 30 sec) and developed with the developer (MF-321, MICROPOSIT, 60 sec). Cu layer (100 nm) is deposited by the e-beam evaporator. After finishing a lift-off process to remove PR masking layer using acetone, SU-8 layer is etched by RIE (CF_4 3 sccm, O_2 81 sccm, 75 mTorr, 100 W, 1 min for four times) in order to open the selected SU-8 region. The Cu mask layer is removed by a wet-etching process (Cu etchant: APS-100, TRANSENE Company INC., 15 sec). The thickness of SU-8 passivation layer is approximately 400 nm by alpha-step 200 profilometer (TENSOR Company).

Next, Chrome (Cr, 10 nm) and Gold (Au, 350 nm) metal electrode are deposited by using the e-beam evaporator. The Cr/Au metal electrode layer is etched by a wet-etching process (Au etchant: TFAC, TRANSENE Company INC., 1 min, Cr etchant: CEP-200, HTA Enterprises, 20 sec) after defining the PR mask (S1827, MICRO CHEM, 4000 rpm, post-baking: 115 ℃ for 1 min, exposure time: 1 min, develop time: 50 sec, hard-baking: 115 ℃ for 5 min) (Figure 2.4.c). RIE (O_2 10 sccm, 10 mTorr, 50 W, 30 sec) process is treated to clean a top surface and remove a photoresist residue for a next fabrication process. Second SU-8 negative photoresist layer for the passivation is spin-coated two times (SU-8 2002, MICRO CHEM, 3000 rpm, 30 sec, ramp up condition, soft-baking: from 65 ℃ to 95 ℃ with slowly warming up for 2 min). The first exposure illumination intensity and time is 12 mW/cm^2 and 15 secs, respectively. After post-baking process at 95 °C for 2 mins, second passivation layer is developed with a developer (AZ 917, 110 sec). The thickness of second SU-8 passivation

layer is approximately 1.5 μm. The fabricated device is taken a hard-baking process at 110 °C for 15 mins (Figure 2.4.d). The fabricated device on the polymer substrate is detached from the handling substrate by anodic metal dissolution method [21,42] (DC power supply E3631A, Agilent, voltage: -25 V ~ 25 V, counter electrode: Pt, electrolyte: Sodium chloride (NaCl), current: 0.657 A) as etching the sacrificial Al layer (Figure 2.4.e). Finally, the integrated μLEDs device for light stimulation as an optoelectronic is fabricated and ready to attach to a graphene-based μECoG device. The detailed information to assemble is described at the end of chapter 2.4 section.

2.4. Fabrication of Graphene-based μECoG device

The fabrication process of graphene-based μECoG device have many steps as reported in our previous papers [26–28]. In this paper, unlike our previous fabrication process, we change the substrate material from Parylene C to PET. Due to excellent optical [43] and biocompatible properties [44], PET was chosen for the transparent substrate instead of Parylene C. The fabrication begins with a preparation of a 4-inch silicon (Si) wafer as a handling substrate that is coated PDMS (ratio: 10:1, 500 rpm, 30 sec, ramp up condition) and baked at 120 °C for 10 mins.

A PET film is attached on the top surface of PDMS/Si substrate (Figure 2.5.a). The PET film is taken an oxygen plasma treatment (RIE, O_2 10 sccm, 10 mTorr, 50 W, 15 sec) to clean the top surface and improve the adhesion of the next SU-8 photoresist layer. Moreover, the handling substrate is coated SU-8 (2002, 3000 rpm, 30 sec, no ramp condition, soft-baking: soft-baking: from 65 °C to 95 °C with slowly warming up for 2 min) layer using a conventional spin-coating method to avoid unexpected unevenness of PET surface. As shown in Figure 2.6, to verify the surface roughness both the bare PET and SU-8/PET film, we measure the surface roughness of them using atomic force microscope (AFM, Bruker Catalyst Bioafm, scan size: 1 × 1 μm^2). The root mean square roughness (Rq) of the bare PET film is 4.84 nm (Figure 2.6.a). On the contrary, the Rq of the coated SU-8 on PET film is 0.93 nm (Figure 2.6.b). The value of Rq on SU-8/PET film is reduced. It also means that the adhesion between SU-8 and the next layer is improved. Connecting traces and pads were formed with metal (Ti: 50 nm, Au: 200 nm) through conventional photolithograph, e-beam evaporation, and lift-off techniques (Figure 2.5.b). The contacting area to a mouse brain of the device is composed to transparent graphene electrode sites. Pristine monolayer graphene is transferred 4 times on the contacting area and the patterned metal traces using a wet transfer technique (Figure 2.5.c). A protective layer 100 nm thick SiO_2 for graphene four sheets was deposited to avoid loss of the graphene in the

further process (Figure 2.5.d). The SiO_2/graphene layers were patterned using conventional photolithography and two steps of dry etching. The first etching step is for SiO_2 layer (RIE, CF_4 45 sccm, O_2 5 sccm, 40 mTorr, 100 W, 4 min) and the second one is for graphene (O_2 10 sccm, 10 mTorr, 50 W, 4 min) (Figure 2.5.e). After the patterned PR was stripped, a second SU-8 (2005) layer was used for encapsulation (Figure 2.5.f). The SU-8 layer was patterned using a metal etching mask (Al, 100 nm) and dry etching process (RIE, CF_4 3 sccm, O_2 81 sccm, 75 mTorr, 100 W, 32 min) in Figure 2.5.g. The Al etching mask is gently etched using AZ 400k developer for 1 min. The fabricated device on PET substrate is detached from PDMS/Si substrate (Figure 2.5.h). Finally, the SiO_2 protection layer is etched using 1:6 buffered oxide etchant (BOE) for 1 min, and the devices were rinsed with DI water (Figure 2.5.i).

Figure 2.4.f shows the attachment process between the backside of both optoelectronic and transparent graphene-based μECoG devices. devices. The 4 × 4 arrays of sixteen μLED are arranged with the top surfaces for emitting a light facing downwards, allowing light to propagate through the same array of transparent graphene-based electrode without obstacles. Each backside polymer substrates of both optical stimulator and transparent signal recording device were combined with an adhesion material NOA 61 (UV exposure time: 90 min).

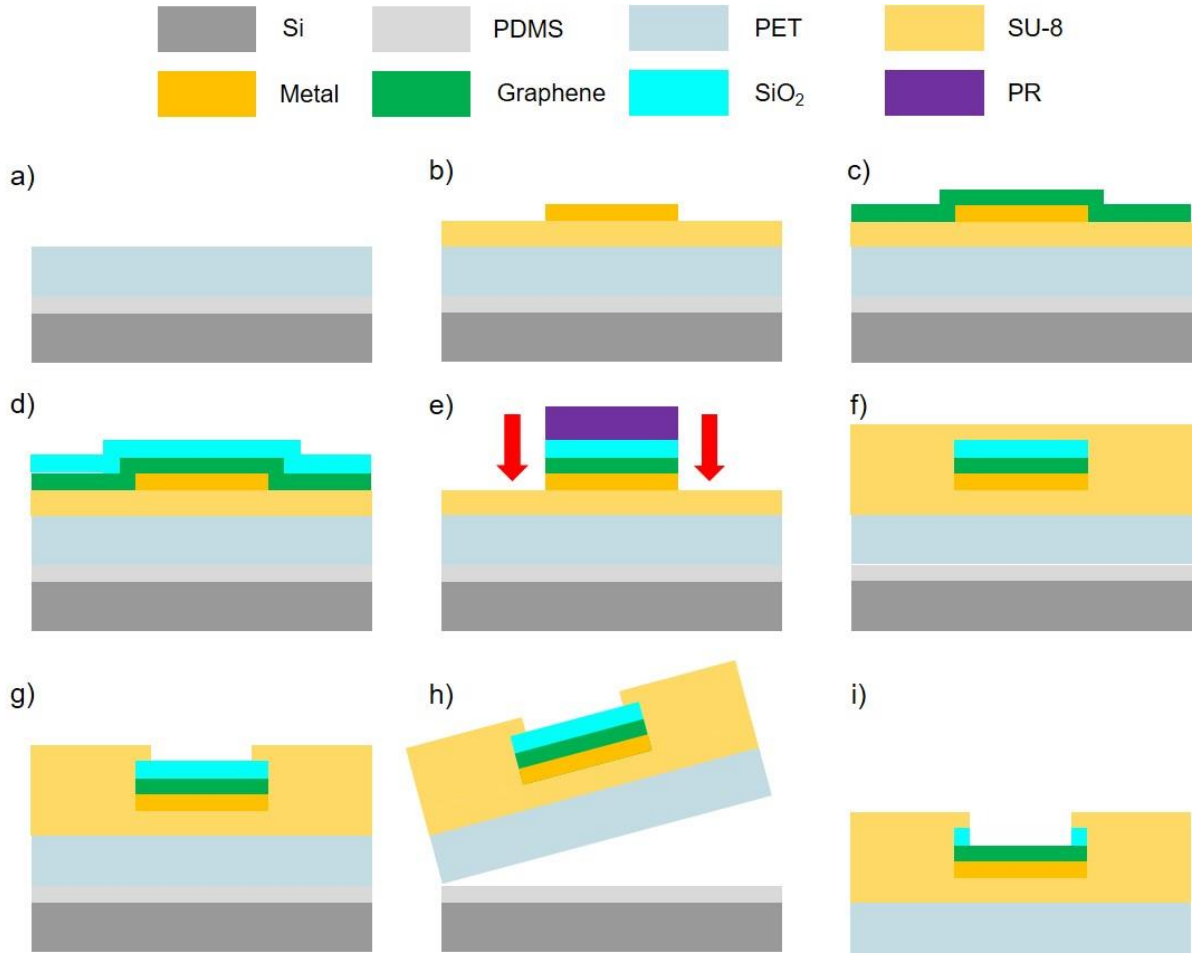

Figure 2.5. Schematic illustration of the fabrication for transparent graphene based μECoG device. a) Attach PET flim on PDMS/Si substrate. b) Coat SU-8 layer and deposit metal traces and pads (Ti/Au). c) Transfer four graphene sheets and d) deposit a protecting layer (SiO_2) on the graphene layers. e) Pattern and etch the graphene layer using RIE. f) Coat a second SU-8 layer for the encapsulation. g) Pattern and etch the top SU-8 layer for opening a recording area site. h) Release the fabricated ECoG device on PDMS/Si substrate and i) etch a SiO2 layer using a buffered oxide etchant.

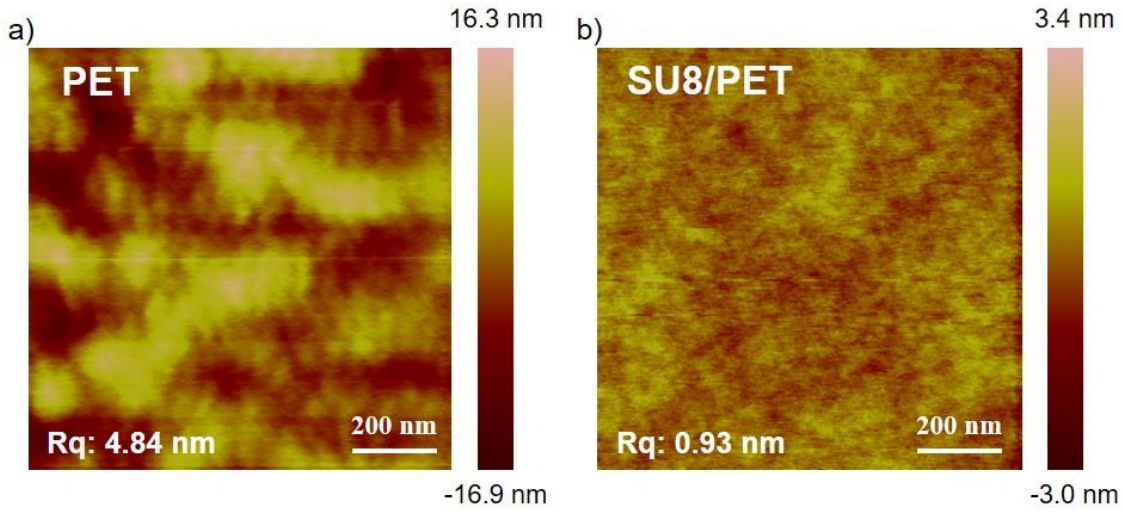

Figure 2.6. Atomic force microscopy (AFM) images on the surface of a) bare PET (Rq: 4.84 nm) and b) SU8/PET (Rq: 0.93 nm) substrate. The scan size is 1 μm × 1 μm.

2.5. Characterization of Optoelectronic device

According the date sheet of the commercial μLED, the emission peak at λ=456.5 is close to the absorption peak of ChR2 at λ=450 nm [41], thus the optoelectronic with μLED array allow to know reasonable technology application for the ChR2 mouse. To evaluate the electrical characteristic of the fabricated μLEDs on the flexible polymer substrate before and after the release process, Current-voltage (I-V) characteristic curve was measured using a semiconductor characterization system (KEITHLEY 4200-SCS, voltage range: 2-3 V, step: 0.03 V, compliance: 0.005 A). The electrode map of the integrated blue μLEDs device is shown in Figure A.1.

Figure 2.7.a shows an average of electrical characteristics of the fabricated 10 μLEDs device with comparison between before (black curve) and after (blue curve) the release process. The bright gray and the dark gray region are each μLEDs component before and after release process, respectively. This is shown that they have the almost same current values during a turn-on state that exceeds 1 mA at approximately 2.7 V. They emitted the blue light and can be applied for the purpose of the light stimulation the optoelectronics.

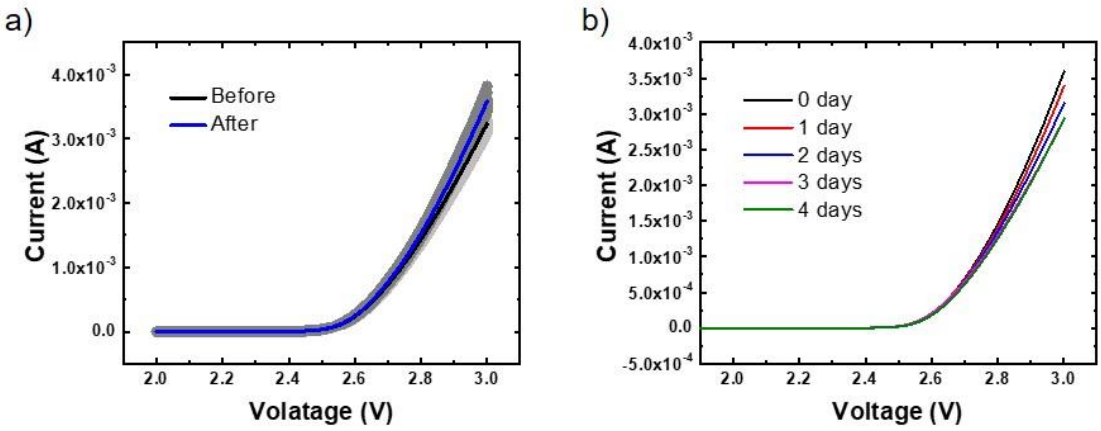

Figure 2.7. Array characterization. a) I-V characteristics of 10 μLEDs between before (black line is average; bright gray is each μLEDs component) and after (blue line is average; dark gray is each μLEDs component) a release process by anodic metal dissolution. The broad twenty gray lines using the two different gray color show I-V characteristics between before and after a release process. b) Average I-V characteristics of 10 μLEDs under the difference soaking times from 0 to 4 days in PBS solution for an accelerated aging test.

Moreover, we performed the accelerated aging test to evaluate the durability and stability of the integrated μLEDs device in a liquid environment as similar as a normal biological environment. The fabricated μLEDs device is soaked in phosphate-buffered saline (PBS, Sigma-Aldrich, 1X, pH 7.4) at 60 °C for 4 days. To match the real situation for the purpose of optogenetic devices, we turned on all of the integrated μLEDs device for a one hour of 24 hours when the device is soaked in PBS at 60 °C. The soaked and fabricated μLEDs device is measured I-V characteristic curve every 24 hours by Autolab PGSTAT 12 (Metrohm Autolab, Netherlands, voltage range: 0-3 V, step: 0.01 V, scan rate: 0.5 V/s).

Accelerated aging test has been widely used for that an artificial procedure for establishing the lifespan or shelf life of medical devices [45]. Accelerated aging experiment

using the Q_{10} (reaction rate coefficient or factor) = 2 rule [46,47] and the Arrhenius equation [48,49] have been also broadly used and applied. Accelerated aging time equation based on Arrhenius equation (Equation 2.1) is written below [45]:

$$Accelerated\ Aging\ Time\ = \frac{Desired\ Real\ Time}{Q10^{\frac{(T1-T0)}{10}}} \qquad \text{(Equation 2.1)}$$

where Q_{10} = reaction rate coefficient, T_1 = Temperature of the reaction (aging), T_0 = Reference or room temperature.

We chose the value of desired real time (2 months, 60 days), T_1 (60 °C) and T^0 (22 °C) to calculate the accelerated aging time for long-term implantation. The calculated accelerated aging time is approximately 4 days. Moreover, all of the μLEDs device is turned on for a one hour during 24 hours for matching the practical application. The real time of the one hour of the accelerated aging time at the same condition is approximately 10 hours. The I-V characteristic curve of the soaked μLEDs device is measured every 24 hours. The I-V curve is shown in Figure 2.7.b. The measurement result shows that the average current values of each accelerated aging days are slightly decreases after soaking. However, after 3 days, the current values are not changed much between 3 and 4 days compared to the one of from 0 to 2 days. This may be due to the soaking device is stabilized at the accelerated aging condition within 2 days. In the results, the μLED arrays retained full functionality with a less degradation of electrical performances in liquid or normal biological environment for the long-term implantation.

2.6. Characterization of Graphene-based μECoG device

2.6.1. Raman Spectroscopy of Graphene layer

Raman spectroscopy (Thermo-Fisher Scientific DXRxi Raman Imaging Microscope) was used to evaluate the quality of a pristine monolayer, four-layer graphene on the Si substrate, and four-layer graphene on a SU8/PET compared to a bare PET film. Raman measurements are carried out using laser source that Raman excitation wavelength is 532 nm at 10.0 mW. The exposure time and number of scans per spectrum are 2.86 msec (350 Hz) and 1000, respectively. The spectral range of Raman shift is from 50 to 3400 cm^{-1}.

Raman spectroscopy is a useful tool to identify and characterize the chemical and physical properties of graphene [50]. Raman spectra of the graphene using 532 nm excitation laser were shown in Figure 2.8.a. For the measurement, the CVD grown graphene layer is transferred using the same wet transfer technique on Si substrate and SU-8/PET substrate, respectively. In general, the single, double, few, and multi layers graphene can be determined by the peak position, peak intensity and peak broadening of Raman spectra. The typical peak positions of graphene are D (1350 cm^{-1}), G (1580 cm^{-1}), and 2D (2690 cm^{-1}) peaks [50]. The graphene has D (1350 cm^{-1}), G (1583 cm^{-1}), and 2D (2673 cm^{-1}) peaks in Figure 2.8.a. The D peak intensity of a monolayer graphene on Si substrate (black line) presents too low to distinguish from near range of conventional D peak. The very low disorder-induced D peak means that the synthesized graphene has the high quality [50]. The intensity ratio of 2D peak over G peak is approximately 2.74. The intensity ratio ($I_{2D}/I_G>2$) means that the graphene is monolayer graphene [51]. Moreover, the ratio of the 2D peak to G peak intensity for four-layer graphene on Si and SU-8/PET were 0.949 and 0.951, respectively. The characterized four-layer graphene on PET substrate also shows C-O, C-C, and C=O bonding of PET at 1290 cm^{-1}, 1614 cm^{-1}, and 1726 cm^{-1}, respectively. These three values are matched the typical peak positions of

a PET material [52–57]. The expanded Raman spectrum (Figure 2.8.a inset) indicates that the G peak was estimated at 1583 cm^{-1} from the four-layer graphene on SU-8/PET substrate.

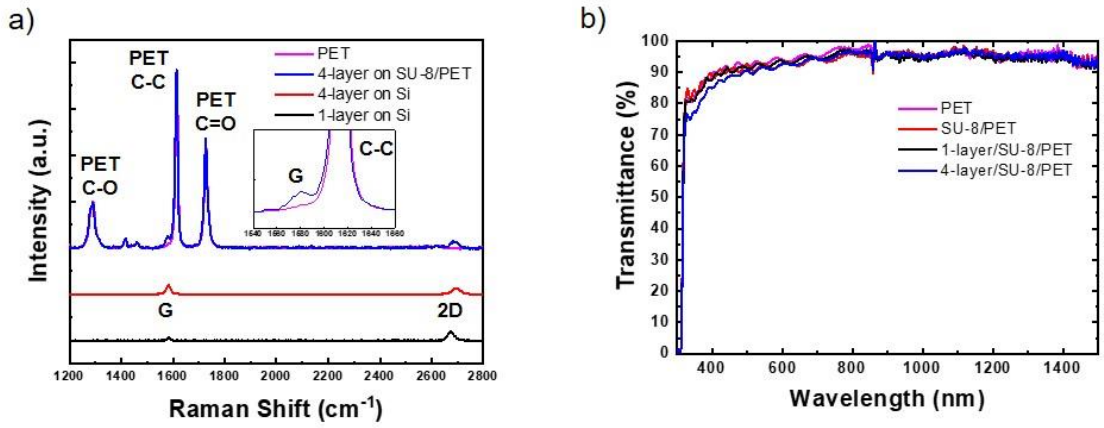

Figure 2.8. a) Raman spectrum of monolayer and four- layer graphene on Si wafer and PET substrate using a 532 nm excitation laser. The ranges are from 1200 to 2800 cm^{-1} and G peak range (inset). Graphene can be identified by the position and shape of its D (1350 cm^{-1}), G (1580 cm^{-1}), and 2D (2690 cm^{-1}) peaks. b) Light Transmittance test results for bare PET, SU8/PET, monolayer graphene on SU8/PET, and four-layer graphene on SU8/PET substrate in UV/VIS wavelength from 300 nm to 1500 nm.

2.6.2. Transmittance

The transmittance of several substrate condition is measured by UV/VIS/NIR spectrometer (Perkin-Elmer Lambda 19). The conditions are a bare PET, SU-8/PET, monolayer graphene/SU-8/PET, and four-layer graphene/SU-8/PET substrates. The wavelength range of the measurement is from 300 nm to 1500 nm. The light sources are deuterium lamp for UV region and halogen lamp for VIS/NIR region.

A graph of the light transmittance versus wavelength for PET, SU-8/PET, monolayer/SU-8/PET, and four-layer/SU-8/PET film is shown Figure 2.8.b. The measurements were taken for the broad range of wavelengths from 300 to 1,500 nm using a UV/VIS/NIR spectrometer. For the four-layer graphene/SU-8/PET as the same device structure, an approximately 90 % of the light impinging on the substrate is transmitted at desired wavelengths (450- 470 nm for excitation of ChR2). This value is similar to previously reported results for optogenetic and neural imaging applications [26,58].

2.6.3. Electrochemical Impedance Spectroscopy (EIS) Measurement

The 16-channel graphene electrode was connected to the Autolab PGSTAT 12 (Metrohm Autolab, Netherlands) via a zero insertion force (ZIF) printed circuit board (PCB) connector. The electrode map of the transparent graphene-based μECoG device is shown in Figure A.2. For the EIS, 500 mV sine waves at frequency from 1 to 100 kHz were used. A three-electrode system was used with graphene-based μECoG as the working electrode (WE), the platinum (Pt) as the counter electrode (CE), and Ag/AgCl as the reference electrode (RE) in saline (LabChem, NaCl, 0.9 % w/v). During the measurement, the fabricated device was soaked in normal saline solution at a room temperature.

Electrochemical impedance spectroscopy is an important tool used to understand the electrochemical performance between a recording electrode and electrolyte interface [59]. The graphene electrodes with the diameters (150 μm) were investigated the impedance property of the graphene-based μECoG. The open surface area of these electrodes is 15,394 μm^2. We measured the electrochemical impedance of transparent graphene-based electrodes using EIS equipment (Figure 2.9). A graphene-based μECoG with fitting and a modeled equivalent circuit (inset) was used to understand its charge-carrying mechanism (Figure 2.9.a). The circuit model includes a solution resistance (R_s), constant phase element impedance (Z_{CPE1}, Z_{CPE2}), Warburg Impedance (Z_W), and charge transfer resistance (R_{CT1}, R_{CT2}). The Nyquist plot exhibits two charge transfer resistance (R_{CT1} = 79.1 kΩ, R_{CT2} = 73.0 MΩ) values, which can be calculated from each semicircle diameter, obtained by fitting with an equivalent circuit. The Z_{CPE} represents the double-layer capacitance of neural electrodes expressed in Equation 2.2 [28], where an ideal capacitor is *n=1*.

$$Z_{CPE} = \frac{1}{Q\omega^n} e^{-(\pi/2)ni} \qquad \text{(Equation 2.2)}$$

where Q is the magnitude of Z_{CPE}, n is a constant ($0 \leq n \leq 1$), and ω is the angular frequency.

The Z_{CPE1} and Z_{CPE2} parameters of the equivalent circuit model are 0.83 $nS \cdot s^{1}$ and 15.8 $nS \cdot s^{0.75}$, respectively. The Bode magnitude and phase plot were used to depict the impedance and phase within 1 to 100 kHz frequency range (Figure 2.9.b-c). The frequency response of impedance for the graphene-based μECoG device showed decreased trend as a function of increasing frequency (Figure 2.9.b). The benchmark frequency of neural electrodes is 1 kHz [60,61]. The average magnitude of the impedance of 16 channels was approximately 161 kΩ at 1 kHz. According to Park et al., they reported the good channels range of electrochemical impedance for four-layer graphene electrode between 100 and 600 kΩ at 1kHz as a function of the various electrode areas [28]. Also, the average phase angle was ~58 º at 1 kHz in Figure 2.9.c. This modeling results shows that the graphene electrodes have a capacitive charge carrying mechanism [59]. Capacitive charge transfer is an essential property for biological stimulation due to the reduced chemical changes and tissue damage that occur at the interface between tissue and electrode.

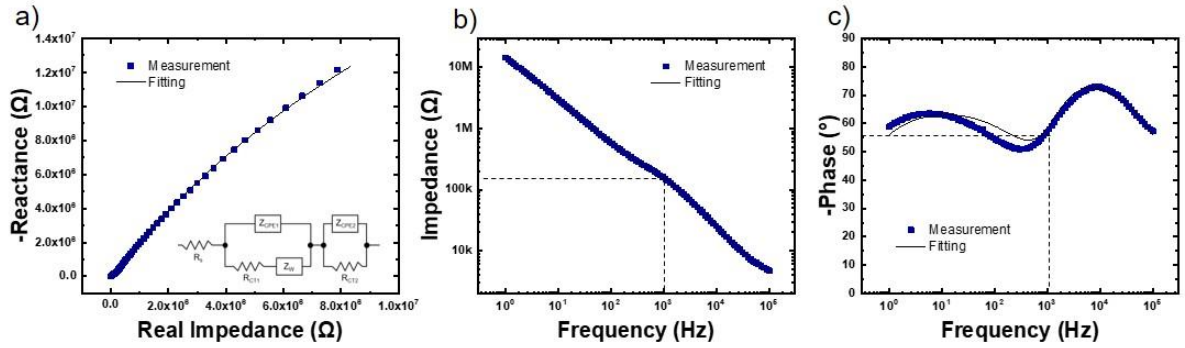

Figure 2.9. a) Nyquist, b) Bode magnitude, and c) Bode phase plot measurement data with fitted model of equivalent circuit (inset) under normal saline (0.9% w/v NaCl) solution.

2.6.4. LED light collimation

The light from LED will expand as it propagates, leading to cross talk between adjac ent recording electrodes. Integrated photonics structures could be used to enhance the collima tion of the beam propagation to reduce the cross talk [62].

2.7. Conclusion

In this study, we demonstrated the fabrication of the combined device between a flexible optoelectronics and transparent graphene-based μECoG electrodes on a flexible substrate for a light stimulation and a neural signal recording, simultaneously. Furthermore, the fabricated device on a flexible polymer substrate allows both a wide range of fabrication procedures to develop biomedical electronic devices and spatially resolution for neural signal recording interfacing with a cerebral cortex. The collimation method of each of μLEDs light due to the light divergence to the μECoG electrodes can be helped and solved to get rid of this issue. Moreover, the fabricated hybrid devices show that they are ready to do the optogenetic experimentation through the graphene-based our device on the cerebral cortex of an animal brain and In-vivo recorded signal characterizations. The application of the fabricated device with optoelectronics and transparent recording electrodes shows the feasibility of this method for developing a biocompatible neuromodulation system with a minimal invasive surgery and fully implantation with the light stimulation and recording devices in the animal brain. Our device has the potential to significantly impact the development of optogenetics devices and could be contributed the next-generation technologies in biomedical electronic area.

2.8. Future Works

2.8.1. Monolithic fabrication and the change of the commercial LEDs

This proposed device in the above section is needed to the separated fabrication process. The one part is the fabrication process of optoelectronics and the other part is the fabrication process of transparent graphene-based μECoG device. Moreover, it needs the attachment process to align the blue LEDs position with the recording electrode area. If we can come up with a monolithic fabrication procedure to make the two devices part in the same batch without the attachment process, it will improve and reduce the fabrication process time and the cost issues, and get rid of the misalignment issue that have a chance during the attachment process by hand. Furthermore, instead of the commercial LEDs, using an epitaxy substrate or materials is helped the reduced the devices size with the same light intensity and wavelength for the target application of optogenetics area and improved the spatial resolution compared to the current device design with the same devices size and area. In addition to, it makes the device to the less invasiveness one with the same spatial resolution.

2.8.2 Combined another LEDs lights for optogenetics such as red, green etc

In this research project, we only used the sixteen blue LEDs array for the optoelectronics to apply the target application, ChR2 mouse model. For the other target model for the optogenetic area, it can be changed and mixed the variable wavelength LEDs array in the one device and the one batch process.

2.8.3. Wireless devices with wireless power transfer (WPT) and NFC modules

We needed the ZIF PCB connector cable to connect the fabricated device to the

measurement equipment such as AutoLab PGSTAT 12 for EIS and Tucker-Davis Technologies (TDT) equipment for the animal experiment to record a neural signal. If we can give and charge the power of the devices and control the each of LEDs using Near Field Communication (NFC) modules, we can make the fully implantable and embedded device in the animal or human body for the neural signal recording application area.

CHAPTER 3. The Implantable Micro-Electrocorticography (μECoG) for Cortical neural interfacing using Cranial Prostheses for the Chronic Implantation.

3.1. Introduction

Many neuroscientists are considered how to be taken benefits of the modular organization and segregation of the cortex in the separated regions and have made tremendous progress understanding how specific computations or mechanisms performed in designated cortical regions involve behavior in recent decades [63–66]. Whatever is happening in the head and nobody really knows, it is not a same computation that performed in the computer. However, despite these interests and curiosity, the analysis of its components in isolated areas can not be understood the performance of the brain.

To better understanding the large-scale brain computations demands the ability to monitor and record neural activity in the large areas of the cortex. In recently, the study of meso- and macro-scopic brain functionality has been used and performed by functional magnetic resonance imaging (fMRI) and magnetoencephalography (MEG) [67,68]. However, fMRI and MEG method are limited by their spatial and temporal resolution [69].

In the recent days, two-photon (2P) imaging to provide the deep imaging has significantly emerged as a tool for in-vivo neural imaging in rodent models compared to one-photon (1P) neural imaging method [70]. Genetically encoded Ca^{2+} indicators, GCaMP6 for the general and well-used method, have enabled and detected in-vivo high-resolution monitoring of hundreds or thousands of neurons activities [71]. Moreover, the other method that is developed red-shifted variants of Ca^{2+} indicators and optogenetic tools make the exploration of deep cortical regions for optical sensing and perturbation [72].

The appearance of new technologies about these new optical tools and equipment for chronic imaging of large-scale areas of the cerebral cortex needs to come up with the replacing

the opaque targeted model skull with a transparent substrate. There are many methods that is researched in the field such as glass coverslips [73], the technique for refractive index matching [74], thinned skull preparation [75], and curved glass windows and their associated surgical implantation methodology [76]. However, those strategies are needed the surgical preparation and is susceptible to the regrowth of the natural animal bone over the time. Recently, the realistic transparent polymer skulls methodology, so called ‘See-Shells’, for long durations (over 300 days) is represented for the large-scale optical access of the dorsal cerebral cortex [77]. They show a practical and feasible technique of this neural image area for replacing an opaque animal cranial bone. However, for the neural signal recording, they used a multi-channel silicon-based neural probe as extracellular recording probe. Therefore, large optical transparent windows with long-term implantation and functionality, easy fabrication and surgical implantation procedure, and flexible design deformation technique are needed.

Here we demonstrate the implantable micro-electrocorticography (μECoG) device for the chronic implantation and allow the internal neural signal recording of the dorsal cerebral cortex of the rodent model.

3.2. Design of the implantable µECoG device

The design of the implantable µECoG device is considered to match the conventional mice brain size and the target 3D-printed cranial prothesis for the long-term implantation. The detailed dimension information is that the diameter of electrode size is 200 µm and the neck length between ZIF connector area and recording area is 5.5 mm. The distance between ECoG sites is approximately 670 µm (Figure 3.1.a). The area of the reference electrode is 2.5 mm (width) × 0.2 mm (length). Figure 3.1.b shows a photograph image of the fabricated µECoG device connected a ZIF PCB connector cable before the animal experiment procedure.

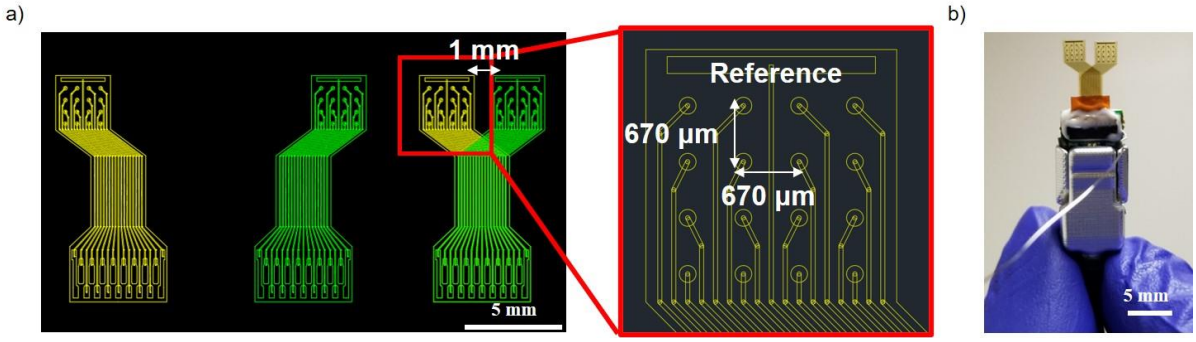

Figure 3.1. The design and photograph images of the fabricated implantable micro-electrocorticography (µECoG) device. a) The design images with the size information. The diameter of electrode size is 200 µm. The neck length is 5.5 mm. The distance between ECoG sites is approximately 670 µm. The area of the reference electrode is 2.5 mm (width) × 0.2 mm (length). b) Photograph image of the fabricated µECoG device connected a ZIF PCB connector.

3.3. Fabrication process of the implantable μECoG device

The implantable μECoG device fabrication process is illustrated in Figure 3.2. Before the fabrication process, a handling substrate is needed to prepare for a stable fabrication procedure when the flexible polymer substrate is used. The handling substrate, 4 inch Si wafer, is prepared by starting a cleaning process. The handling substate is cleaned and washed by ultrasonication with acetone, isopropyl alcohol (IPA), and deionized water (AQUA SOLUTIONS, resistance: 18 M Ω). After that cleaning process, the 4 inch wafer is dried at 110 °C for 1 min on a hot plate prior to use. For the release process in a further fabrication process, aluminum (Al, 30 nm) layer is deposited on the pre-cleaned handling substrate by an e-beam evaporator (Vacuum deposition system, ANGSTROM ENINEERING, 2×10^{-6} Torr). The handling substrate is ready to use for the fabrication process of the implantable μECoG device. As shown in Figure 3.2.a, the 1st polyimide (PI, HD4110, HD MicroSystems, 2500 rpm, 40 sec, ramp up condition) layer is spin-coated on the pre-cleaned handling substrate. The 1st PI layer is soft-baked at 90 °C for 6 mins and 110 °C for 6 mins, respectively. The soft-baked 1st PI layer is patterned to define the shape of the proposed device by a conventional lithography process using Suss MA6 Aligner equipment (365 nm, 10 mW/cm^2, 40 sec). The exposed sample is undergone a post exposure bake (PEB) process at 110 °C for 90 secs. The patterned sample is developed by the proper developer (PA401D, HD Microsystems, 3 min) and rinse solution (PA400R, HD Microsystems, 1 min), respectively. In the sequence, the patterned sample is hard-baked in a cooke vacuum annealer equipment (Cooke Vacuum Products, 375 °C, 4 Torr for Nitrogen process gas). The thickness of the cured and patterned PI layer is approximately 15 μm. The metal electrode (Titanium, Ti, 30 nm/Gold, Au, 230 nm) is deposited by using the e-beam evaporator after defined the photoresist (PR) mask (KL1604, KemLab, 2500 rpm for 30 sec, soft-baking: 110 °C for 60 sec, exposure time: 13 sec, PEB: 115 °C for 60 sec, development time: 90 sec using the mixed solution both MF^{TM}-CD-26,

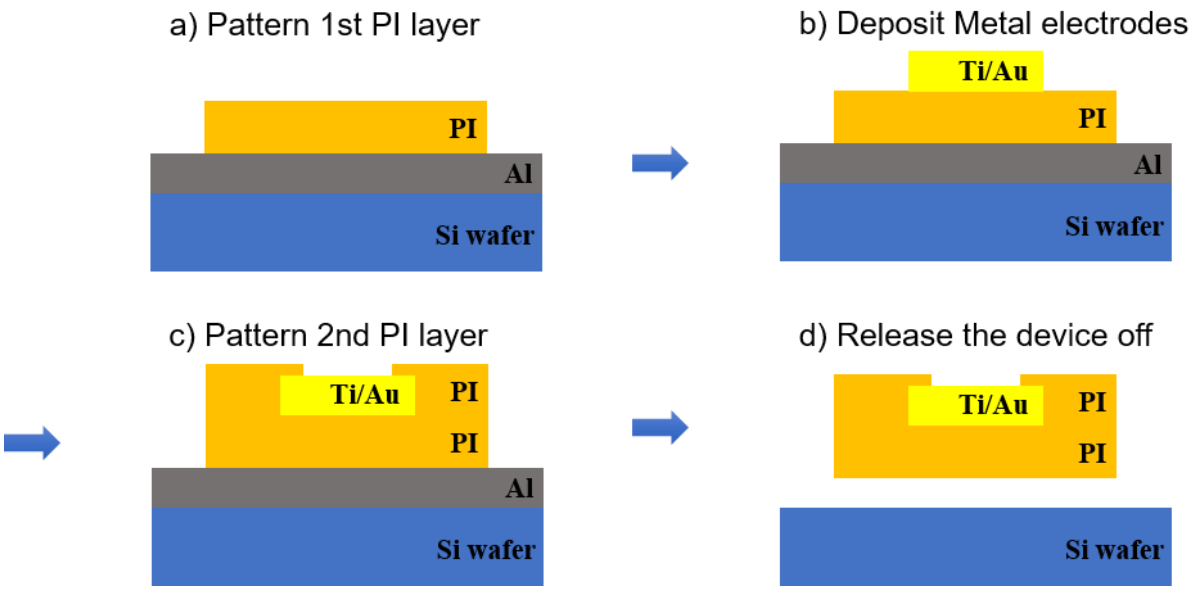

Figure 3.2. Schematic illustration of the fabrication process for the implantable micro-electrocorticography (μECoG) devices. a) Pattern 1st polyimide (PI) layer on a handling substrate by a photolithography process using MA6 aligner equipment. b) Deposit metal electrodes on 1st PI layer by a conventional e-beam evaporator. c) Pattern 2nd PI layer using the same process of 1st PI layer. d) Release the fabricated device on the handling substrate to each a sacrificial layer, Al, by a wet-etching process.

Microposit™, 100 mL and a deionized water, 75 mL) as shown in Figure 3.2.b. The thickness of PR layer is around 3 μm. Oxygen plasma treatment (Reactive ion etching, RIE, O_2 10 sccm, 10 mTorr, 50 W, 30 sec) process is treated to clean a top surface and remove a photoresist residue for a stable next fabrication process before the PR coating and metal deposition processes, respectively. After a conventional life-off process using acetone, 2nd PI layer as a passivation layer is coated and patterned by the same method of the 1st PI layer (Figure 3.2.c). As shown in Figure 3.2.d, the fabricated device on the handling substate is detached by a wet-etching process (AZ400K developer, MicroChemicals) to remove the sacrificial layer (Al). The fabricated device is successfully released from the handling substrate without any issues and problem.

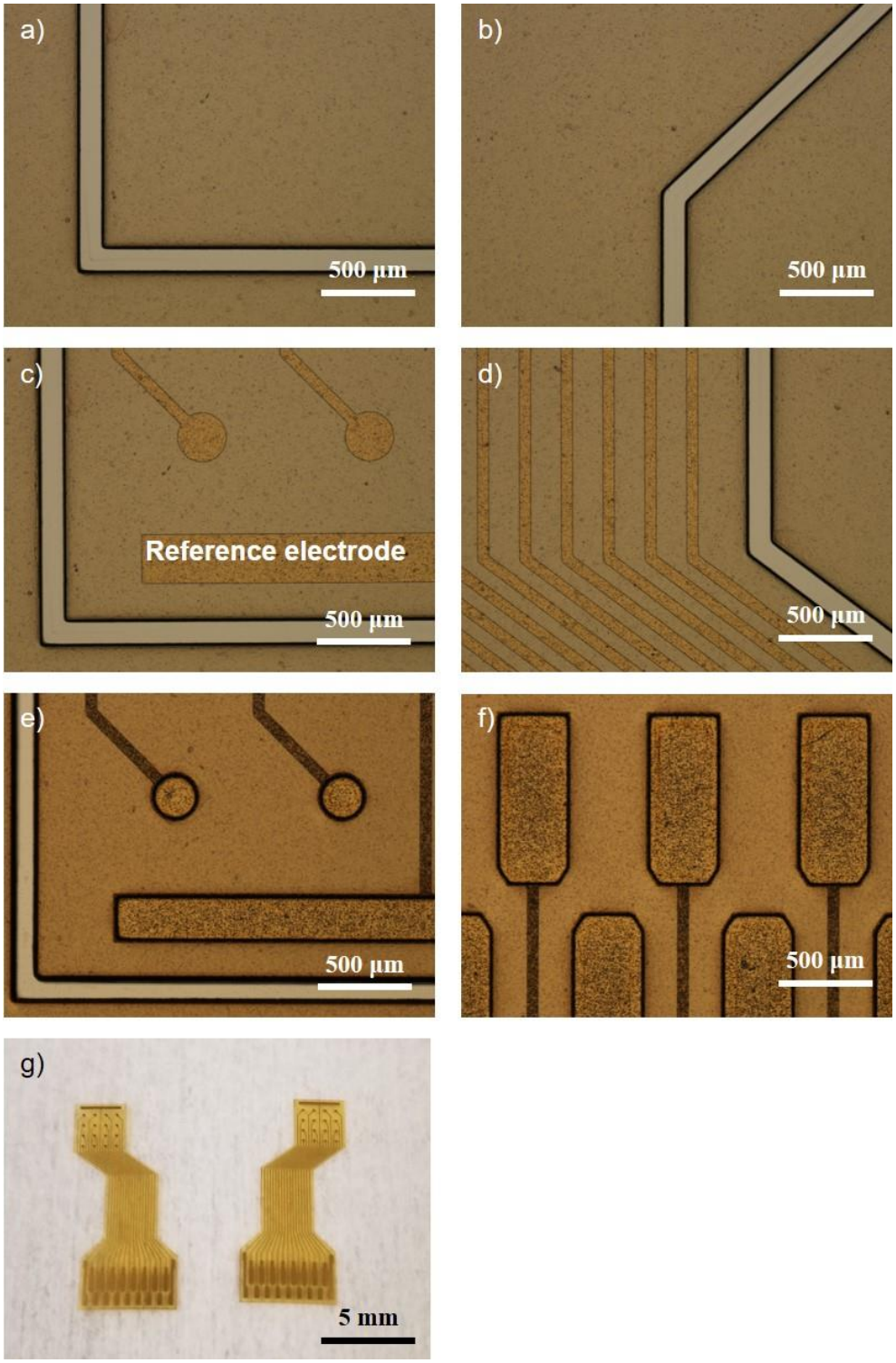

Figure 3.3. Corresponding samples microscopy and photograph images based on the fabrication flow. a-b) Pattern 1st PI layer. c-d) Deposit metal electrodes. e-f) Pattern 2nd PI layer. g) The release the device off from the handling substrate.

The microscopy and photograph of corresponding samples as followed the fabrication process are shown in Figure 3.3. The 1st PI layer for the substrate is defined well in Figure 3.3.a-b. The metal electrodes are deposited on the 1st PI substrate after a lift-off process using acetone in Figure 3.3.c-d. Moreover, the gap between the device area and outside of the device is clear and there is no PR residue in the gap. It is good for the next fabrication step. The 2nd PI layer as a passivation layer is patterned and cured in a cooke vacuum annealer equipment in Figure 3.3.e-f. The fabricated device is released from the handling substrate using a wet etching process to remove a sacrificial (Al) layer in Figure 3.3.g. After finished the washing and dry process, the fabricated devices are well defined and made as followed the predicted and designed fabrication procedure.

3.4. Device characterization

The implantable μECoG device is measured the electrochemical impedance spectroscopy (EIS) of the metal electrodes with the diameters (200 μm) by AutoLab PGSTAT 12 with the connection using a zero insertion force (ZIF) printed circuit board (PCB) connector. The frequency range is from 1 to 100 kHz and a three-electrode system was applied with an implanted μECoG electrode as a working electrode (WE), the platinum (Pt) as a counter electrode (CE), and Ag/AgCl as a reference electrode (RE) in phosphate-buffered saline (PBS). The electrodes maps of the integrated μECoG device are shown in Figure B.1. Left-side and right-side devices are connected 1-32 headstage channel cable between ZIF connector and the recording equipment for measuring a neural or electrical signal. The fabricated device is soaked in PBS solution at a room temperature when the device is measured. The electrode open area of the implantable μECoG device is 25,447 μm^2. The measurement results of left-side and right-side devices is shown in Figure 3.4. The Bode magnitude and phase plot were used to depict the impedance and phase within the measurement frequency condition. The benchmark frequency for the neural electrodes is 1 kHz [60,61]. Compared to the other researcher reference using a metal electrode [78], the fabricated devices that have the impedance around 15 kΩ at 1 kHz have good channels for the target application area in Figure 3.4.a,c. Also, the average of phase angle both of devices at 1 kHz is approximately 70 ° in Figure 3.4.b-d. This Bode phase plot measurement means that the metal electrodes have a capacitive charge carrying mechanism [59]. For the bio application area, the capacitive charge transfer property is and essential because of the reduced chemical changes and tissue damage that generated on the interface between the tissue and electrode.

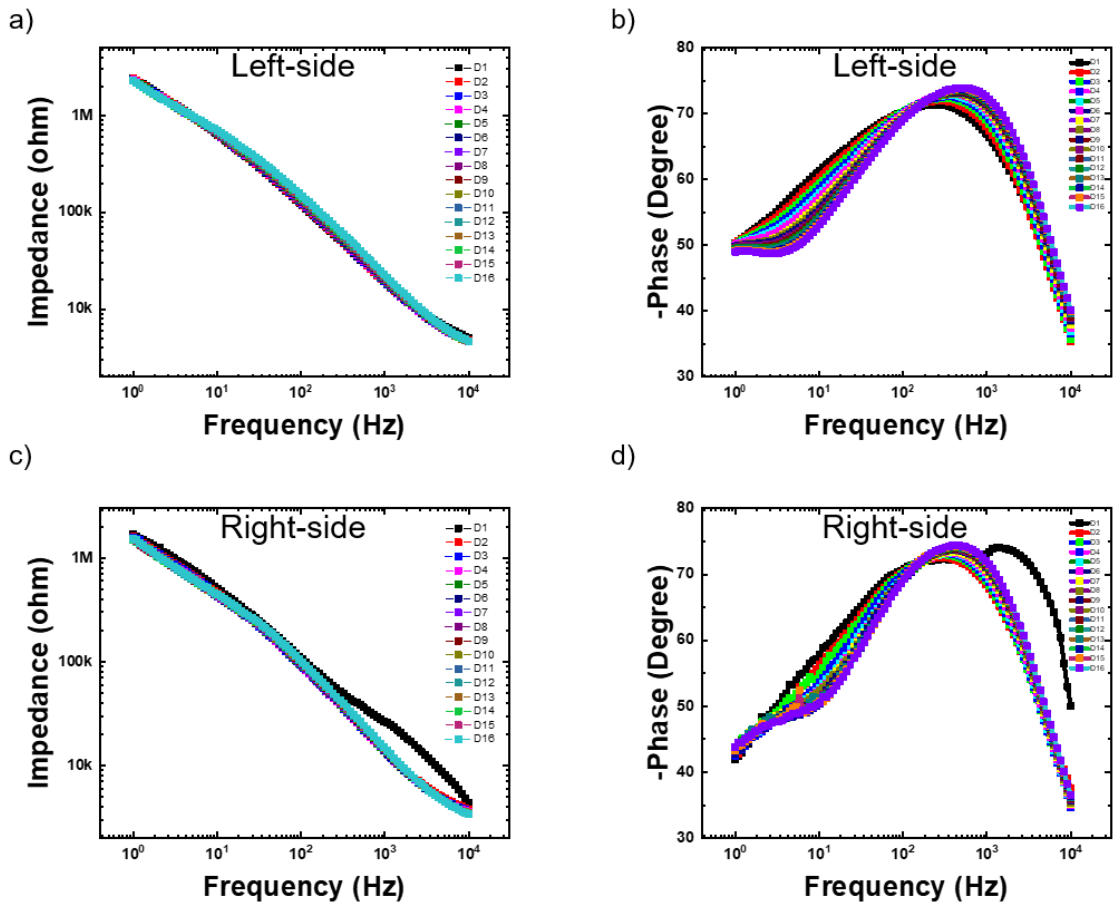

Figure 3.4. Electrochemical impedance spectroscopy (EIS) measurement results. a, c) Bode magnitude and b, d) Bode phase plot measurement results of the left-side and right-side devices, respectively.

3.5. Animal experiment using cranial prostheses for the chronic implantation

The fabricated μECoG device is conducted the implantation process on the brain tissue of an acute mice. The animal experiment is started the hold process to fix the mice brain position for the autodrill process on the stage (Figure 3.5.a). After shaving and incise the mice brain area skin in Figure 3.5.b, we measured the X-Y-Z coordinate of the cranial bone location and input this information in the program that is made by Stephan Blanz. The drill is pathed the designated position as a function of the heights step by step. When the drill is down to the targeted Z axis position, the mice brain can be removed from the brain. The fabricated device is connected the recording equipment using a ZIF PCB and headstage cable and implanted on the top surface of the opened mice brain (Figure 3.5.c). In Figure 3.5.d, the enlarged photograph image shows that the fabricated devices are implanted and touched the top surface of the mice brain model. We know that this implantation method is needed to modify and improve the procedure to establish the long-term implantation. This is a first time to conduct the real animal experiment using the first sample that is a invented and fabricated devices. We need to figure out the modification of the device and the implantation method in the further related research.

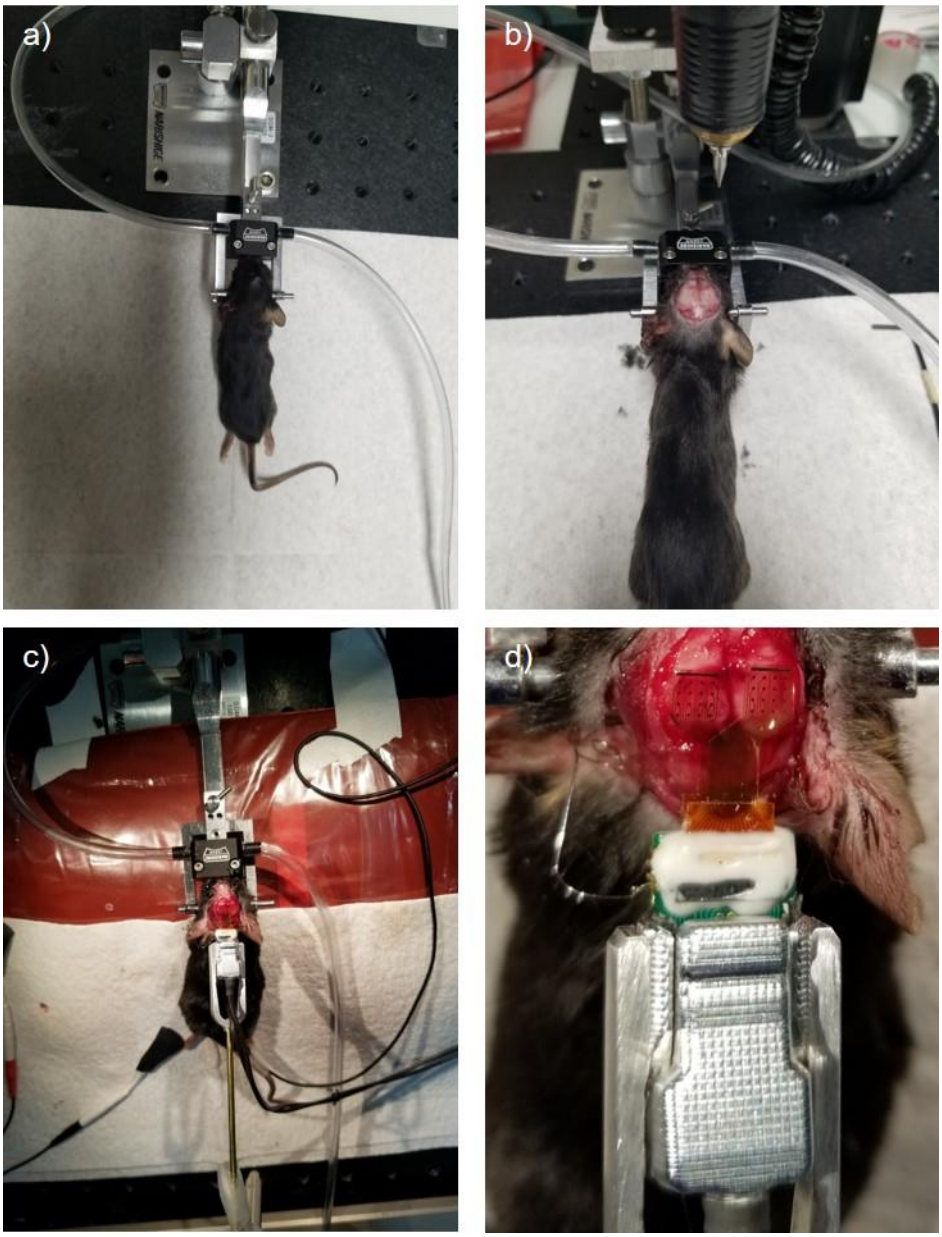

Figure 3.5. Photograph images of animal experiment procedure for the implantation process. a) Hold the mice head on the stage. b) Incise the mice brain area skin, drill, and remove the cranial bone using the designed and programed autodriller machine by Stephan Blanz. c) Test the attachment and implantation process without a cranial prothesis at that moment. d) Enlarged a photograph image when the device is attached on the brain surface.

3.6. Conclusion

In this study, we demonstrated the implantable μECoG device to apply the chronic implantation and make the device recording of the neural signal of the dorsal cerebral cortex of the rodent model without external recording probe. The photocurable PI substrate allows the stable mechanical property of the fabricated device. Moreover, the proposed device has the stable and easy fabrication procedure. Compared to fMRI and MEG application areas, our device has a good spatial and temporal resolution. Moreover, the EIS measurement result shows that all μECoG electrodes are fully working and ready to record the neural signal of the rodent brain surface. Furthermore, we also conducted and shows the possibility of the long-term chronic implantation procedure with the acute rodent model with the autodriller machine to open the cranial bone from the rodent. We also figured out the improvement of the current implantation method for the chronic implantation procedure. The detailed information of the future works is shown in the next section (Chapter 3.7). Our device has the potential to apply and impact the internal neural signal recording application and the neural image research fields.

3.7. Future works

3.7.1. The transparent substrate for the neural imaging research field

The photocurable polyimide (PI, HD4100) is not a transparent material but a yellowish one. This color works for the current research purpose. However, for the future study of the neural imaging area, we need to figure out whether this photocurable PI material is a proper one or not. Figure 3.6 shows the fluorescence microscopy images of the photocurable PI in the green fluorescent protein (GFP) and TxRed fluorescent channel taken by Dr. Kevin P. Cheng. The device light up pretty brightly in those channels. It means that the photocurable PI emit an autofluorescence in GFP and TxRed channels. Especially in the GFP channel is that the normal method is the use for GCaMP. As the results, the photocurable PI is not appliable in the neural imaging area. We need the other candidate materials to match the neural imaging area.

We have searched the other candidate materials. The one of the candidate materials is CP1 transparent polyimide (PI, NeXolve Holding company, CP1 in resin form in Diglyme). We conducted the curing process of the CP1 transparent PI in a cooke vacuum annealer. Moreover, the cured CP1 layer is captured the fluorescence microscopy images in the same channels (Figure 3.7). Based on the images in Figure 3.7.a-d, the CP1 PI is much clear and transparent compared to the photocurable PI in the GFP and TxRed channels. To better understanding, we also check the Parylene C material that our group used to use the device substrate for the bio application area in the past. The CP1 PI and Parylene C substrate put side by side in brightfield, GFP, and TxRed channels (Figure 3.7.e-g), respectively. Compared to Parylene C material, CP1 PI material have some autofluorescence in both channels whereas the parylene C is completely clear in the TxRed Channel. CP1 PI material might be the proper materials to do the conventional semiconductor fabrication. However, we found that the CPI PI material is susceptible to acetone and affected the solution that contains N-Methyl-2-

Pyrrolidone (NMP) solvent and extremely polar solvents such as THF, DMAc, DMF. As a result, we continually needed to find the proper stable materials for the neural imaging and the conventional semiconductor fabrication process.

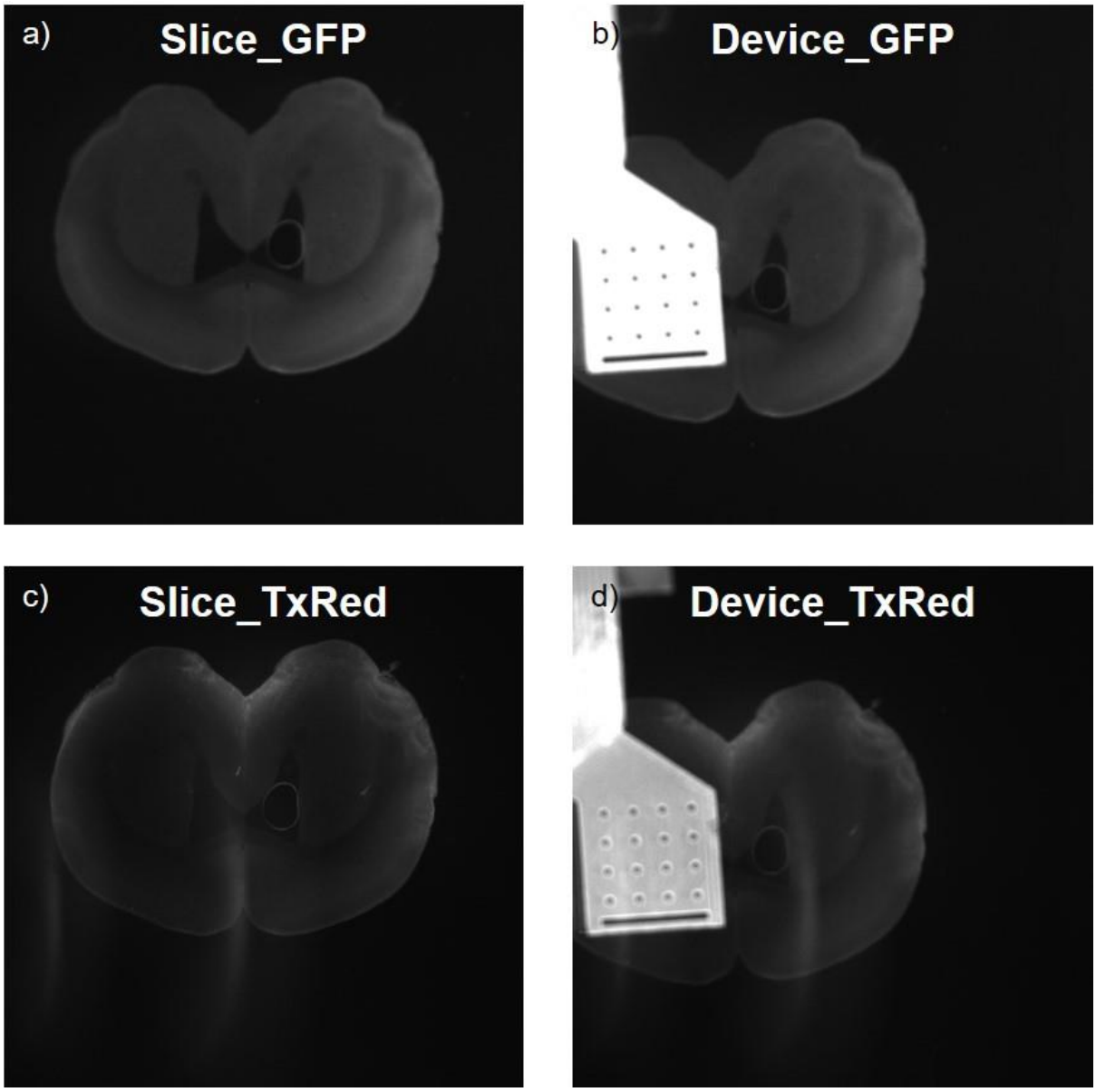

Figure 3.6. Fluorescence microscopy images of photocurable polyimide (PI) by taken Kevin P. Cheng. a) A slice in the green fluorescent protein (GFP) channel and b) put the device over top of the slide. c) A slice in the TxRed fluorescent channel and d) put the device over top of the slide. The devices light up pretty brightly. Especially in the GFP channel which is the one we normally use for GCaMP.

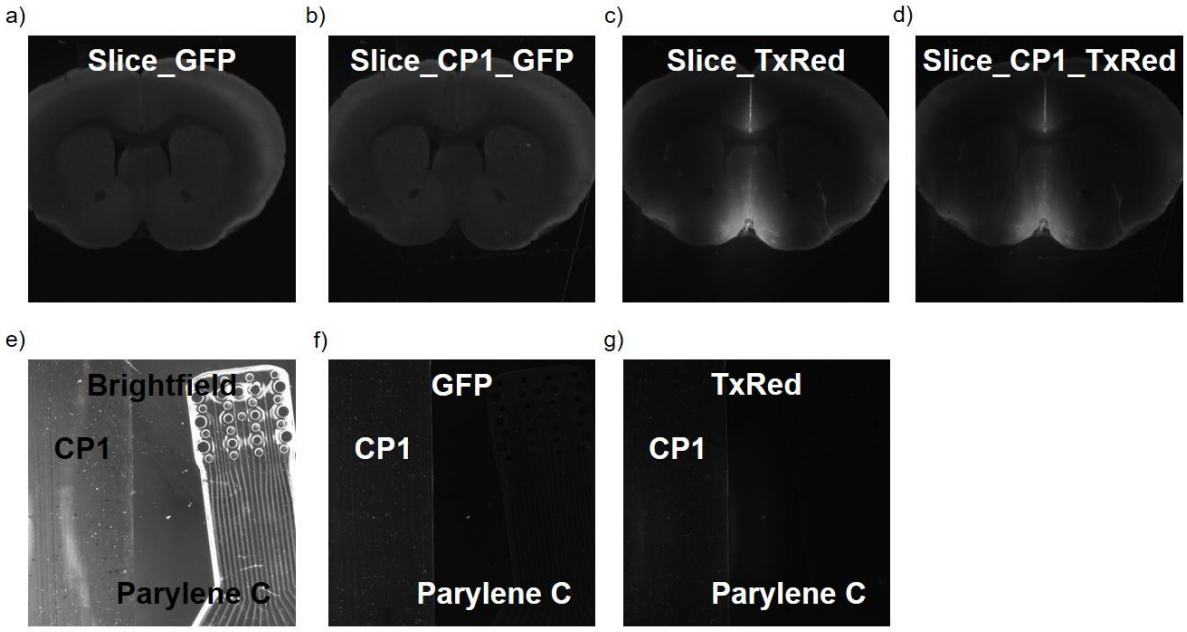

Figure 3.7. Fluorescence microscopy images of CP1 transparent polyimide (PI) by taken Kevin P. Cheng. a) A slice in the GFP channel and b) put the device over top of slide. c) A slice in the TxRed fluorescent channel and d) put the device over top of the slide. e) Put the CP1 transparent PI and Parylene C substrates side by side in brightfield, f) GFP channel, and g) TxRed channel. Compared to Parylene C material, CP1 PI material have some autofluorescence in both channels whereas the Parylene C is completely clear in the TxRed Channel.

3.7.2 The implantation method for the long-term implantation

The photograph images of the cranial prothesis are shown in Figure C.1. The cranial prothesis is made by 3D-printer using polymethylmethacrylate (PMMA) and Titanium (Ti). The surface of the 3D-printed frame is boned the flexible polyethylene terephthalate, PET, film as a real device substrate (Figure C.1.a,c-d). Titanium head plate to support the stable mechanical property is shown in Figure C.1.b. These two frames will be assembled in the final stage on the implantation process in the future. This concept is given from the other research group in department of mechanical engineering at University of Minnesota. Moreover they published the concept so called ‘See-shell’ in the journal [77]. We are collaborating this concept research and will be made the improved concept devices.

CHAPTER 4. Conclusion

4.1. Conclusion

A design and fabrication of the combined device between optoelectronics for light simulation and transparent graphene-based μECoG electrodes for neural signal recording is the first topic in this thesis. Prior to introducing the main idea, the related concepts and methods of optogenetics and the development of ECoG field are reviewed in the introduction section. In this topic, we choose the usage of the commercial blue LEDs for the light stimulation of the target ChR2 mouse model. The detailed fabrication and measurement results is written in sequence followed the related chapters. In the optogenetics field, the designed and fabricated current device concept have a potential to apply those area for a target wavelength stimulation to the genetically encoded rodent model and human in the future. The future research and works to improve the current device concept are investigated and written in the end of chapter 2.

The implantable μECoG for cortical neural interfacing using 3D-printed cranial prostheses for the chronic implantation methodology is the second topic of this thesis. The demonstrated device can be also applied the chronic implantation procedure and allow the internal neural signal recording of the dorsal cerebral cortex of the rodent model. Our device has a better spatial and temporal resolution than the fMRI and MEG application areas. The specific information of fabrication procedure and the presented chronic implantation method is also described in the certain chapter. As same as the first topic, the improvement of proposed device concept and the chronic implantation methodology for the neural imaging area are written in the end of chapter 3.

4.2. Suggestions for Future Works

Future works of the first and second topic is written in the end of each chapters.

The new research project will include developing a functional magnetic resonance imaging (fMRI) compatible electrode device. The other researchers are reported that the metal electrode, especially Platinum, and traces make an artifact that the MRI are blur in the metal region. We fabricated the test sample using platinum and four-layer graphene electrodes to compare the fMRI image result, separately. The taken fMRI shows that there is not the artifact between platinum as the metal electrode and four-layer graphene as the transparent electrode. Both are transparent in the fMRI capture condition. Based on the test results, we will only use the metal electrode for the next experiment. The research purpose is the chronic implantation for non-human primates. The research topic has a chance to give us an applicable high-quality medical recording methodology.

BIBLIOGRAPHY

1. Deisseroth, K.; Feng, G.; Majewska, A.K.; Miesenböck, G.; Ting, A.; Schnitzer, M.J. Next-Generation Optical Technologies for Illuminating Genetically Targeted Brain Circuits. *J. Neurosci.* **2006**, *26*, 10380–10386, doi:10.1523/JNEUROSCI.3863-06.2006.
2. Mukerjee, S.; Lazartigues, E. Next-Generation Tools to Study Autonomic Regulation In Vivo. *Neurosci. Bull.* **2019**, *35*, 113–123, doi:10.1007/s12264-018-0319-2.
3. Albert, D.; Block, A.; Bruce, B.; Haines, D.; McCloskey, L.; Mitchell, R.; Moore, K.; Petri, W.; Telser, A. *Dorland's Illustrated Medical Dictionary*; Philadelphia: Elsevier Saunders, 2012;
4. Xu, X.; Mee, T.; Jia, X. New Era of Optogenetics: From the Central to Peripheral Nervous System. *Critical Reviews in Biochemistry and Molecular Biology* **2020**, *55*, 1–16, doi:10.1080/10409238.2020.1726279.
5. Guru, A.; Post, R.J.; Ho, Y.-Y.; Warden, M.R. Making Sense of Optogenetics. *Int J Neuropsychopharmacol* **2015**, *18*, doi:10.1093/ijnp/pyv079.
6. Eickelbeck, D.; Karapinar, R.; Herlitze, S.; Spoida, K. Chapter 16 - Optogenetic Approaches for Controlling Neuronal Activity and Plasticity. In *Handbook of Behavioral Neuroscience*; Manahan-Vaughan, D., Ed.; Handbook of Neural Plasticity Techniques; Elsevier, 2018; Vol. 28, pp. 285–310.
7. Govorunova, E.G.; Sineshchekov, O.A.; Li, H.; Spudich, J.L. Microbial Rhodopsins: Diversity, Mechanisms, and Optogenetic Applications. *Annual Review of Biochemistry* **2017**, *86*, 845–872, doi:10.1146/annurev-biochem-101910-144233.
8. Zhang, F.; Vierock, J.; Yizhar, O.; Fenno, L.E.; Tsunoda, S.; Kianianmomeni, A.; Prigge, M.; Berndt, A.; Cushman, J.; Polle, J.; et al. The Microbial Opsin Family of Optogenetic Tools. *Cell* **2011**, *147*, 1446–1457, doi:10.1016/j.cell.2011.12.004.
9. Bayraktar, H.; Fields, A.P.; Kralj, J.M.; Spudich, J.L.; Rothschild, K.J.; Cohen, A.E. Ultrasensitive Measurements of Microbial Rhodopsin Photocycles Using Photochromic FRET. *Photochemistry and Photobiology* **2012**, *88*, 90–97, doi:https://doi.org/10.1111/j.1751-1097.2011.01011.x.
10. Ernst, O.P.; Lodowski, D.T.; Elstner, M.; Hegemann, P.; Brown, L.S.; Kandori, H. Microbial and Animal Rhodopsins: Structures, Functions, and Molecular Mechanisms. *Chem. Rev.* **2014**, *114*, 126–163, doi:10.1021/cr4003769.
11. Shokoueinejad, M.; Park, D.-W.; Jung, Y.H.; Brodnick, S.K.; Novello, J.; Dingle, A.; Swanson, K.I.; Baek, D.-H.; Suminski, A.J.; Lake, W.B.; et al. Progress in the Field of Micro-Electrocorticography. *Micromachines* **2019**, *10*, 62, doi:10.3390/mi10010062.
12. Wang, W.; Degenhart, A.D.; Collinger, J.L.; Vinjamuri, R.; Sudre, G.P.; Adelson, P.D.; Holder, D.L.; Leuthardt, E.C.; Moran, D.W.; Boninger, M.L.; et al. Human Motor Cortical Activity Recorded with Micro-ECoG Electrodes, during Individual Finger Movements. In Proceedings of the 2009 Annual International Conference of the IEEE Engineering in Medicine and Biology Society; September 2009; pp. 586–589.
13. *Stretchable Bioelectronics for Medical Devices and Systems*; Rogers, J.A., Ghaffari, R., Kim, D.-H., Eds.; Microsystems and Nanosystems; Springer International Publishing: Cham, 2016; ISBN 978-3-319-28692-1.
14. Rogers, J.A.; Someya, T.; Huang, Y. Materials and Mechanics for Stretchable Electronics. *Science* **2010**, *327*, 1603–1607, doi:10.1126/science.1182383.
15. Kim, D.-H.; Ghaffari, R.; Lu, N.; Rogers, J.A. Flexible and Stretchable Electronics for Biointegrated Devices. *Annu. Rev. Biomed. Eng.* **2012**, *14*, 113–128, doi:10.1146/annurev-bioeng-071811-150018.
16. Liu, Y.; Pharr, M.; Salvatore, G.A. Lab-on-Skin: A Review of Flexible and Stretchable Electronics for Wearable Health Monitoring. *ACS Nano* **2017**, *11*, 9614–9635, doi:10.1021/acsnano.7b04898.
17. Yun, S.O.; Hwang, Y.; Park, J.; Jeong, Y.; Kim, S.H.; Noh, B.I.; Jung, H.S.; Jang, H.S.; Hyun, Y.; Choa, S.-H.; et al. Sticker-Type Alq3-Based OLEDs Based on Printable Ultrathin Substrates in Periodically Anchored and Suspended Configurations. *Advanced Materials* **2013**, *25*, 5626–5631, doi:10.1002/adma201302503.
18. Park, S.I.; Brenner, D.S.; Shin, G.; Morgan, C.D.; Copits, B.A.; Chung, H.U.; Pullen, M.Y.; Noh, K.N.; Davidson, S.; Oh, S.J.; et al. Soft, Stretchable, Fully Implantable Miniaturized Optoelectronic Systems for Wireless Optogenetics. *Nature Biotechnology* **2015**, *33*, 1280–1286, doi:10.1038/nbt.3415.
19. Noh, K.N.; Park, S.I.; Qazi, R.; Zou, Z.; Mickle, A.D.; Grajales-Reyes, J.G.; Jang, K.-I.; Gereau, R.W.; Xiao, J.; Rogers, J.A.; et al. Miniaturized, Battery-Free Optofluidic Systems with Potential for Wireless Pharmacology and Optogenetics. *Small* **2018**, *14*, 1702479, doi:10.1002/smll.201702479.
20. Fenno, L.; Yizhar, O.; Deisseroth, K. The Development and Application of Optogenetics. *Annual Review of Neuroscience* **2011**, *34*, 389–412, doi:10.1146/annurev-neuro-061010-113817.
21. Thongpang, S.; Richner, T.J.; Brodnick, S.K.; Schendel, A.; Kim, J.; Wilson, J.A.; Hippensteel, J.; Krugner-Higby, L.; Moran, D.; Ahmed, A.S.; et al. A Micro-Electrocorticography Platform and Deployment Strategies for Chronic BCI Applications. *Clin EEG Neurosci* **2011**, *42*, 259–265, doi:10.1177/155005941104200412.
22. Henle, C.; Raab, M.; Cordeiro, J.G.; Doostkam, S.; Schulze-Bonhage, A.; Stieglitz, T.; Rickert, J. First Long Term in Vivo Study on Subdurally Implanted Micro-ECoG Electrodes, Manufactured with a Novel Laser

Technology. *Biomed Microdevices* **2011**, *13*, 59–68, doi:10.1007/s10544-010-9471-9.
23. Viventi, J.; Kim, D.-H.; Vigeland, L.; Frechette, E.S.; Blanco, J.A.; Kim, Y.-S.; Avrin, A.E.; Tiruvadi, V.R.; Hwang, S.-W.; Vanleer, A.C.; et al. Flexible, Foldable, Actively Multiplexed, High-Density Electrode Array for Mapping Brain Activity in Vivo. *Nature Neuroscience* **2011**, *14*, 1599–1605, doi:10.1038/nn.2973.
24. Rubehn, B.; Bosman, C.; Oostenveld, R.; Fries, P.; Stieglitz, T. A MEMS-Based Flexible Multichannel ECoG-Electrode Array. *J. Neural Eng.* **2009**, *6*, 036003, doi:10.1088/1741-2560/6/3/036003.
25. Kuzum, D.; Takano, H.; Shim, E.; Reed, J.C.; Juul, H.; Richardson, A.G.; de Vries, J.; Bink, H.; Dichter, M.A.; Lucas, T.H.; et al. Transparent and Flexible Low Noise Graphene Electrodes for Simultaneous Electrophysiology and Neuroimaging. *Nature Communications* **2014**, *5*, 1–10, doi:10.1038/ncomms6259.
26. Park, D.-W.; Schendel, A.A.; Mikael, S.; Brodnick, S.K.; Richner, T.J.; Ness, J.P.; Hayat, M.R.; Atry, F.; Frye, S.T.; Pashaie, R.; et al. Graphene-Based Carbon-Layered Electrode Array Technology for Neural Imaging and Optogenetic Applications. *Nature Communications* **2014**, *5*, 1–11, doi:10.1038/ncomms6258.
27. Park, D.-W.; Brodnick, S.K.; Ness, J.P.; Atry, F.; Krugner-Higby, L.; Sandberg, A.; Mikael, S.; Richner, T.J.; Novello, J.; Kim, H.; et al. Fabrication and Utility of a Transparent Graphene Neural Electrode Array for Electrophysiology, in Vivo Imaging, and Optogenetics. *Nature Protocols* **2016**, *11*, 2201–2222, doi:10.1038/nprot.2016.127.
28. Park, D.-W.; Ness, J.P.; Brodnick, S.K.; Esquibel, C.; Novello, J.; Atry, F.; Baek, D.-H.; Kim, H.; Bong, J.; Swanson, K.I.; et al. Electrical Neural Stimulation and Simultaneous in Vivo Monitoring with Transparent Graphene Electrode Arrays Implanted in GCaMP6f Mice. *ACS Nano* **2018**, *12*, 148–157, doi:10.1021/acsnano.7b04321.
29. Chen, H.; Müller, M.B.; Gilmore, K.J.; Wallace, G.G.; Li, D. Mechanically Strong, Electrically Conductive, and Biocompatible Graphene Paper. *Advanced Materials* **2008**, *20*, 3557–3561, doi:10.1002/adma.200800757.
30. Bonaccorso, F.; Sun, Z.; Hasan, T.; Ferrari, A.C. Graphene Photonics and Optoelectronics. *Nature Photonics* **2010**, *4*, 611–622, doi:10.1038/nphoton.2010.186.
31. Sparta, D.R.; Stamatakis, A.M.; Phillips, J.L.; Hovelsø, N.; van Zessen, R.; Stuber, G.D. Construction of Implantable Optical Fibers for Long-Term Optogenetic Manipulation of Neural Circuits. *Nature Protocols* **2012**, *7*, 12–23, doi:10.1038/nprot.2011.413.
32. Clements, I.P.; Gnade, A.G.; Rush, A.D.; Patten, C.D.; Twomey, M.C.; Kravitz, A.V. Miniaturized LED Sources for in Vivo Optogenetic Experimentation. In Proceedings of the Optogenetics: Optical Methods for Cellular Control; International Society for Optics and Photonics, March 8 2013; Vol. 8586, p. 85860X.
33. Ji, B.; Wang, M.; Kang, X.; Gu, X.; Li, C.; Yang, B.; Wang, X.; Liu, J. Flexible Optoelectric Neural Interface Integrated Wire-Bonding μ LEDs and Microelectrocorticography for Optogenetics. *IEEE Transactions on Electron Devices* **2017**, *64*, 2008–2015, doi:10.1109/TED.2016.2645860.
34. Ji, B.; Guo, Z.; Wang, M.; Yang, B.; Wang, X.; Li, W.; Liu, J. Flexible Polyimide-Based Hybrid Opto-Electric Neural Interface with 16 Channels of Micro-LEDs and Electrodes. *Microsystems & Nanoengineering* **2018**, *4*, 1–11, doi:10.1038/s41378-018-0027-0.
35. Kwon, K.Y.; Sirowatka, B.; Weber, A.; Li, W. Opto-MECoG Array: A Hybrid Neural Interface With Transparent MECoG Electrode Array and Integrated LEDs for Optogenetics. *IEEE Transactions on Biomedical Circuits and Systems* **2013**, *7*, 593–600, doi:10.1109/TBCAS.2013.2282318.
36. Zorzos, A.N.; Scholvin, J.; Boyden, E.S.; Fonstad, C.G. Three-Dimensional Multiwaveguide Probe Array for Light Delivery to Distributed Brain Circuits. *Opt. Lett., OL* **2012**, *37*, 4841–4843, doi:10.1364/OL.37.004841.
37. Lee, J.; Ozden, I.; Song, Y.-K.; Nurmikko, A.V. Transparent Intracortical Microprobe Array for Simultaneous Spatiotemporal Optical Stimulation and Multichannel Electrical Recording. *Nature Methods* **2015**, *12*, 1157–1162, doi:10.1038/nmeth.3620.
38. Mao, D.; Morley, J.; Zhang, Z.; Donnelly, M.; Xu, G. High-Yield Passive Si Photodiode Array Towards Optical Neural Recording. *IEEE Electron Device Letters* **2018**, *39*, 524–527, doi:10.1109/LED.2018.2802451.
39. Mao, D.; Li, N.; Xiong, Z.; Sun, Y.; Xu, G. Single-Cell Optogenetic Control of Calcium Signaling with a High-Density Micro-LED Array. *iScience* **2019**, *21*, 403–412, doi:10.1016/j.isci.2019.10.024.
40. Reddy, J.W.; Kimukin, I.; Towe, E.; Chamanzar, M. Flexible, Monolithic, High-Density MLED Neural Probes for Simultaneous Optogenetics Stimulation and Recording*. In Proceedings of the 2019 9th International IEEE/EMBS Conference on Neural Engineering (NER); March 2019; pp. 831–834.
41. Prabhakar, A.; Vujovic, D.; Cui, L.; Olson, W.; Luo, W. Leaky Expression of Channelrhodopsin-2 (ChR2) in Ai32 Mouse Lines. *PLOS ONE* **2019**, *14*, e0213326, doi:10.1371/journal.pone.0213326.
42. Metz, S.; Bertsch, A.; Renaud, P. Partial Release and Detachment of Microfabricated Metal and Polymer Structures by Anodic Metal Dissolution. *Journal of Microelectromechanical Systems* **2005**, *14*, 383–391, doi:10.1109/JMEMS.2004.839328.
43. Faraj, M.G.; Ibrahim, K.; Ali, M.K.M. PET as a Plastic Substrate for the Flexible Optoelectronic Applications. 5.

44. Khan, W.; Muntimadugu, E.; Jaffe, M.; Domb, A.J. Implantable Medical Devices. In *Focal Controlled Drug Delivery*; Domb, A.J., Khan, W., Eds.; Advances in Delivery Science and Technology; Springer US: Boston, MA, 2014; pp. 33–59 ISBN 978-1-4614-9434-8.
45. Lambert, B.J.; Tang, F.-W. Rationale for Practical Medical Device Accelerated Aging Programs in AAMI TIR 17. *Radiation Physics and Chemistry* **2000**, *57*, 349–353, doi:10.1016/S0969-806X(99)00403-X.
46. Reich, R.R.; Sharpe, D.C.; Anderson, H.D. Accelerated Aging of Packaging: Considerations, Suggestions, and Use in Expiration Date Verification. *Med Dev Diag Ind* **1988**, *10*, 34.
47. Carfagno, S.P.; Gibson, R.J. *A Review of Equipment Aging Theory and Technology*; Electric Power Research Institute, 1980;
48. Clough, R.L.; Gillen, K.T.; Campan, J.L.; Gaussens, G.; Schönbacher, H.; Seguchi, T.; Wilski, H.; Machi, S. Plant Safety. *Nuclear safety* **1984**, *25*, 238.
49. Edell, D.J. Insulating Biomaterials Research for Implantable Microelectronic Devices. *MRS Online Proceedings Library (OPL)* **2003**, *773*, doi:10.1557/PROC-773-N1.9.
50. Jaureguib, L.A.; Parkb, W.; Caoa, H.; Chena, Y.P.; Childres, I.; Jauregui, L.A.; Park, W.; Al, E. *Raman Spectroscopy of Graphene and Related Materials*;
51. Cao, H.; Yu, Q.; Jauregui, L.A.; Tian, J.; Wu, W.; Liu, Z.; Jalilian, R.; Benjamin, D.K.; Jiang, Z.; Bao, J.; et al. Electronic Transport in Chemical Vapor Deposited Graphene Synthesized on Cu: Quantum Hall Effect and Weak Localization. *Appl. Phys. Lett.* **2010**, *96*, 122106, doi:10.1063/1.3371684.
52. Lesko, C.C.C.; Rabolt, J.F.; Ikeda, R.M.; Chase, B.; Kennedy, A. Experimental Determination of the Fiber Orientation Parameters and the Raman Tensor of the 1614cm−1 Band of Poly(Ethylene Terephthalate). *Journal of Molecular Structure* **2000**, *521*, 127–136, doi:10.1016/S0022-2860(99)00430-5.
53. Colomban, Ph.; Herrera Ramirez, J.M.; Paquin, R.; Marcellan, A.; Bunsell, A. Micro-Raman Study of the Fatigue and Fracture Behaviour of Single PA66 Fibres: Comparison with Single PET and PP Fibres. *Engineering Fracture Mechanics* **2006**, *73*, 2463–2475, doi:10.1016/j.engfracmech.2006.04.033.
54. Ni, Z.H.; Yu, T.; Lu, Y.H.; Wang, Y.Y.; Feng, Y.P.; Shen, Z.X. Uniaxial Strain on Graphene: Raman Spectroscopy Study and Band-Gap Opening. *ACS Nano* **2008**, *2*, 2301–2305, doi:10.1021/nn800459e.
55. Rebollar, E.; Pérez, S.; Hernández, M.; Domingo, C.; Martín, M.; A. Ezquerra, T.; P. García-Ruiz, J.; Castillejo, M. Physicochemical Modifications Accompanying UV Laser Induced Surface Structures on Poly(Ethylene Terephthalate) and Their Effect on Adhesion of Mesenchymal Cells. *Physical Chemistry Chemical Physics* **2014**, *16*, 17551–17559, doi:10.1039/C4CP02434F.
56. Liu, Y.; Liu, Y.; Qin, S.; Xu, Y.; Zhang, R.; Wang, F. Graphene-Carbon Nanotube Hybrid Films for High-Performance Flexible Photodetectors. *Nano Res.* **2017**, *10*, 1880–1887, doi:10.1007/s12274-016-1370-9.
57. Farber, C.; Li, J.; Hager, E.; Chemelewski, R.; Mullet, J.; Rogachev, A.Yu.; Kurouski, D. Complementarity of Raman and Infrared Spectroscopy for Structural Characterization of Plant Epicuticular Waxes. *ACS Omega* **2019**, *4*, 3700–3707, doi:10.1021/acsomega.8b03675.
58. Kim, K.S.; Zhao, Y.; Jang, H.; Lee, S.Y.; Kim, J.M.; Kim, K.S.; Ahn, J.-H.; Kim, P.; Choi, J.-Y.; Hong, B.H. Large-Scale Pattern Growth of Graphene Films for Stretchable Transparent Electrodes. *Nature* **2009**, *457*, 706–710, doi:10.1038/nature07719.
59. Cogan, S.F. Neural Stimulation and Recording Electrodes. *Annual Review of Biomedical Engineering* **2008**, *10*, 275–309, doi:10.1146/annurev.bioeng.10.061807.160518.
60. Williams, J.C.; Hippensteel, J.A.; Dilgen, J.; Shain, W.; Kipke, D.R. Complex Impedance Spectroscopy for Monitoring Tissue Responses to Inserted Neural Implants. *J. Neural Eng.* **2007**, *4*, 410–423, doi:10.1088/1741-2560/4/4/007.
61. Norlin, P.; Kindlundh, M.; Mouroux, A.; Yoshida, K.; Hofmann, U.G. A 32-Site Neural Recording Probe Fabricated by DRIE of SOI Substrates. *J. Micromech. Microeng.* **2002**, *12*, 414–419, doi:10.1088/0960-1317/12/4/312.
62. Kosaka, H.; Kawashima, T.; Tomita, A.; Notomi, M.; Tamamura, T.; Sato, T.; Kawakami, S. Self-Collimating Phenomena in Photonic Crystals. *Appl. Phys. Lett.* **1999**, *74*, 1212–1214, doi:10.1063/1.123502.
63. Yamamoto, H.; Moriya, S.; Ide, K.; Hayakawa, T.; Akima, H.; Sato, S.; Kubota, S.; Tanii, T.; Niwano, M.; Teller, S.; et al. Impact of Modular Organization on Dynamical Richness in Cortical Networks. *Science Advances* **2018**, *4*, eaau4914, doi:10.1126/sciadv.aau4914.
64. Read, H.L.; Winer, J.A.; Schreiner, C.E. Modular Organization of Intrinsic Connections Associated with Spectral Tuning in Cat Auditory Cortex. *PNAS* **2001**, *98*, 8042–8047, doi:10.1073/pnas.131591898.
65. Schreiner, C.E.; Read, H.L.; Sutter, M.L. Modular Organization of Frequency Integration in Primary Auditory Cortex. *Annual Review of Neuroscience* **2000**, *23*, 501–529, doi:10.1146/annurev.neuro.23.1.501.
66. G, V.; Y, S.; Ra, P.; B, G.; D, B.; Jb, P.; B, T. Atlases of Cognition with Large-Scale Human Brain Mapping. *PLoS Comput Biol* **2018**, *14*, e1006565–e1006565, doi:10.1371/journal.pcbi.1006565.
67. Koepp, M.; Caciagli, L.; Kane, E.; Sone, D. The Basics: What Constitutes a Photoparoxysmal Response? FMRI, PET, TMS and MEG Studies. In *The Importance of Photosensitivity for Epilepsy*; Kasteleijn-Nolst Trenite, D., Ed.; Springer International Publishing: Cham, 2021; pp. 199–205 ISBN 978-3-319-05080-5.

68. Rossi, E.; Dussias, P.E.; Diaz, M.; van Hell, J.G.; Newman, S. Neural Signatures of Inhibitory Control in Intra-Sentential Code-Switching: Evidence from FMRI. *Journal of Neurolinguistics* **2021**, *57*, 100938, doi:10.1016/j.jneuroling.2020.100938.
69. Thukral, A.; Ershad, F.; Enan, N.; Rao, Z.; Yu, C. Soft Ultrathin Silicon Electronics for Soft Neural Interfaces: A Review of Recent Advances of Soft Neural Interfaces Based on Ultrathin Silicon. *IEEE Nanotechnology Magazine* **2018**, *12*, 21–34, doi:10.1109/MNANO.2017.2781290.
70. Centonze, V.E.; White, J.G. Multiphoton Excitation Provides Optical Sections from Deeper within Scattering Specimens than Confocal Imaging. *Biophysical Journal* **1998**, *75*, 2015–2024, doi:10.1016/S0006-3495(98)77643-X.
71. Chen, T.-W.; Wardill, T.J.; Sun, Y.; Pulver, S.R.; Renninger, S.L.; Baohan, A.; Schreiter, E.R.; Kerr, R.A.; Orger, M.B.; Jayaraman, V.; et al. Ultrasensitive Fluorescent Proteins for Imaging Neuronal Activity. *Nature* **2013**, *499*, 295–300, doi:10.1038/nature12354.
72. Akerboom, J.; Carreras Calderón, N.; Tian, L.; Wabnig, S.; Prigge, M.; Tolö, J.; Gordus, A.; Orger, M.B.; Severi, K.E.; Macklin, J.J.; et al. Genetically Encoded Calcium Indicators for Multi-Color Neural Activity Imaging and Combination with Optogenetics. *Front. Mol. Neurosci.* **2013**, *6*, doi:10.3389/fnmol.2013.00002.
73. Holtmaat, A.; Paola, V. de; Wilbrecht, L.; Trachtenberg, J.T.; Svoboda, K.; Portera-Cailliau, C. Imaging Neocortical Neurons through a Chronic Cranial Window. *Cold Spring Harb Protoc* **2012**, *2012*, pdb.prot069617, doi:10.1101/pdb.prot069617.
74. Silasi, G.; Xiao, D.; Vanni, M.P.; Chen, A.C.N.; Murphy, T.H. Intact Skull Chronic Windows for Mesoscopic Wide-Field Imaging in Awake Mice. *Journal of Neuroscience Methods* **2016**, *267*, 141–149, doi:10.1016/j.jneumeth.2016.04.012.
75. Drew, P.J.; Shih, A.Y.; Driscoll, J.D.; Knutsen, P.M.; Blinder, P.; Davalos, D.; Akassoglou, K.; Tsai, P.S.; Kleinfeld, D. Chronic Optical Access through a Polished and Reinforced Thinned Skull. *Nature Methods* **2010**, *7*, 981–984, doi:10.1038/nmeth.1530.
76. Kim, T.H.; Zhang, Y.; Lecoq, J.; Jung, J.C.; Li, J.; Zeng, H.; Niell, C.M.; Schnitzer, M.J. Long-Term Optical Access to an Estimated One Million Neurons in the Live Mouse Cortex. *Cell Reports* **2016**, *17*, 3385–3394, doi:10.1016/j.celrep.2016.12.004.
77. Ghanbari, L.; Carter, R.E.; Rynes, M.L.; Dominguez, J.; Chen, G.; Naik, A.; Hu, J.; Sagar, M.A.K.; Haltom, L.; Mossazghi, N.; et al. Cortex-Wide Neural Interfacing via Transparent Polymer Skulls. *Nature Communications* **2019**, *10*, 1500, doi:10.1038/s41467-019-09488-0.
78. Bong, J.; Attia, Z.I.; Vaidya, V.R.; Jung, Y.H.; Padmanabhan, D.; Lee, J.; Kim, H.; Ladewig, D.J.; Noseworthy, P.A.; Asirvatham, S.J.; et al. Radiolucent Implantable Electrocardiographic Monitoring Device Based on Graphene. *Carbon* **2019**, *152*, 946–953, doi:10.1016/j.carbon.2019.06.069.

Appendix A. Electrode maps of the integrated blue µLEDs and transparent graphene-based µECoG device

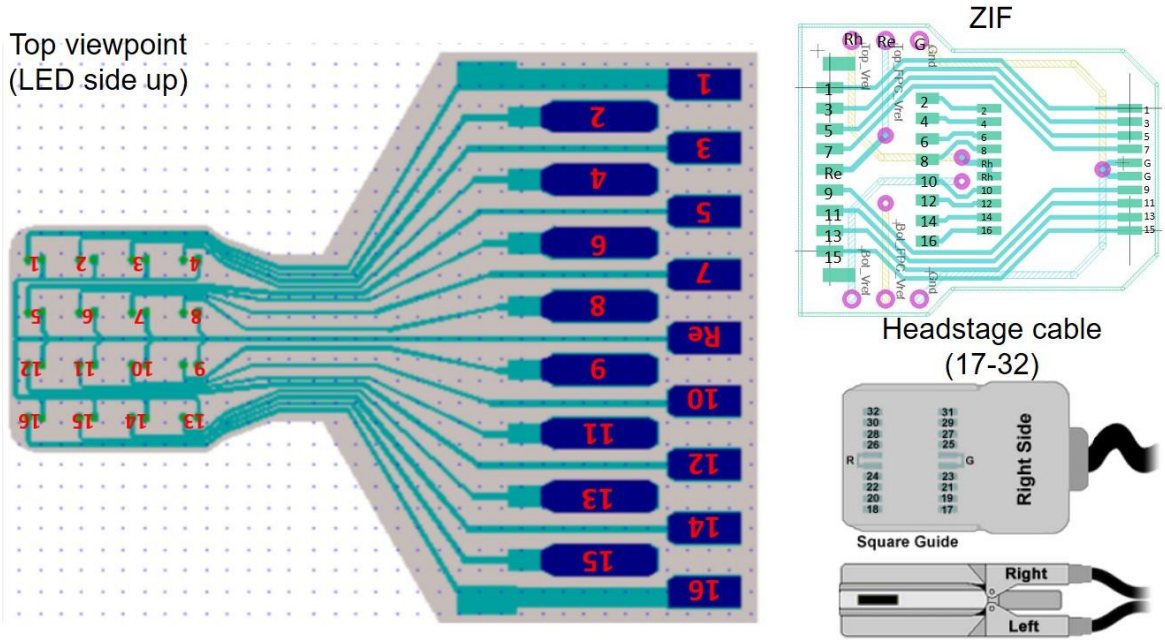

Figure A.1. Electrode maps of the integrated blue µLEDs device. Connected 17-32 headstage channel cable between LED control box and LED's ZIF connector.

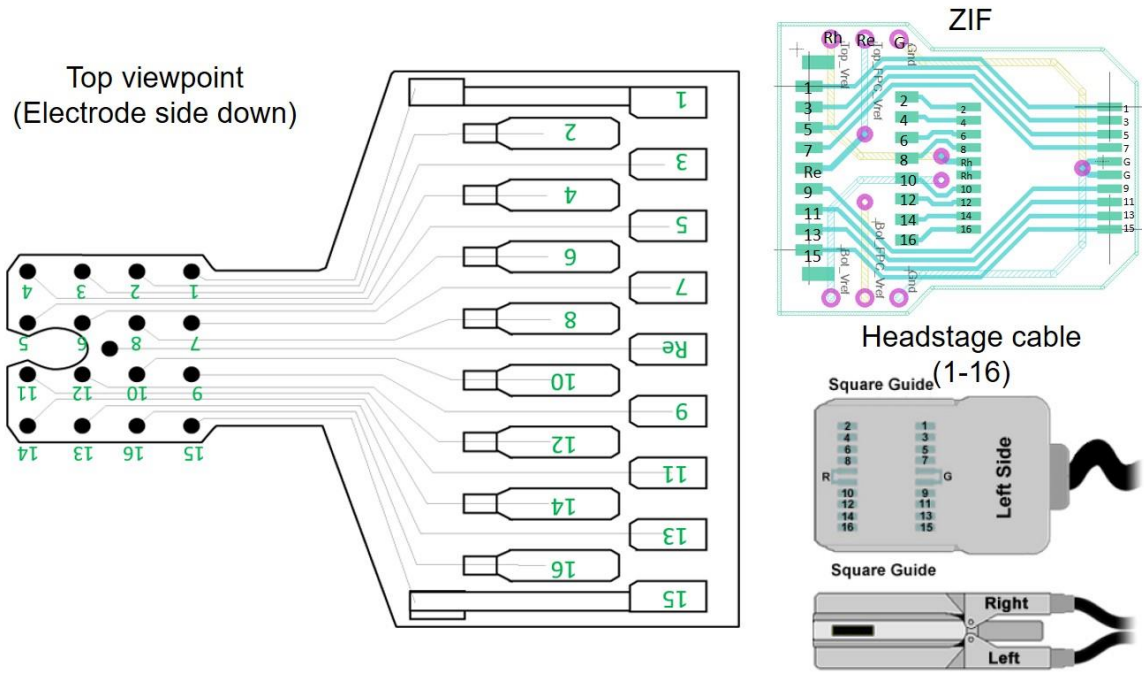

Figure A.2. Electrode maps of the transparent graphene-based µECoG device. Connected 1-16 channel cable between PZ5-32 and graphene-based ECoG's ZIF connector.

Appendix B. Electrode maps of the implantable μECoG device

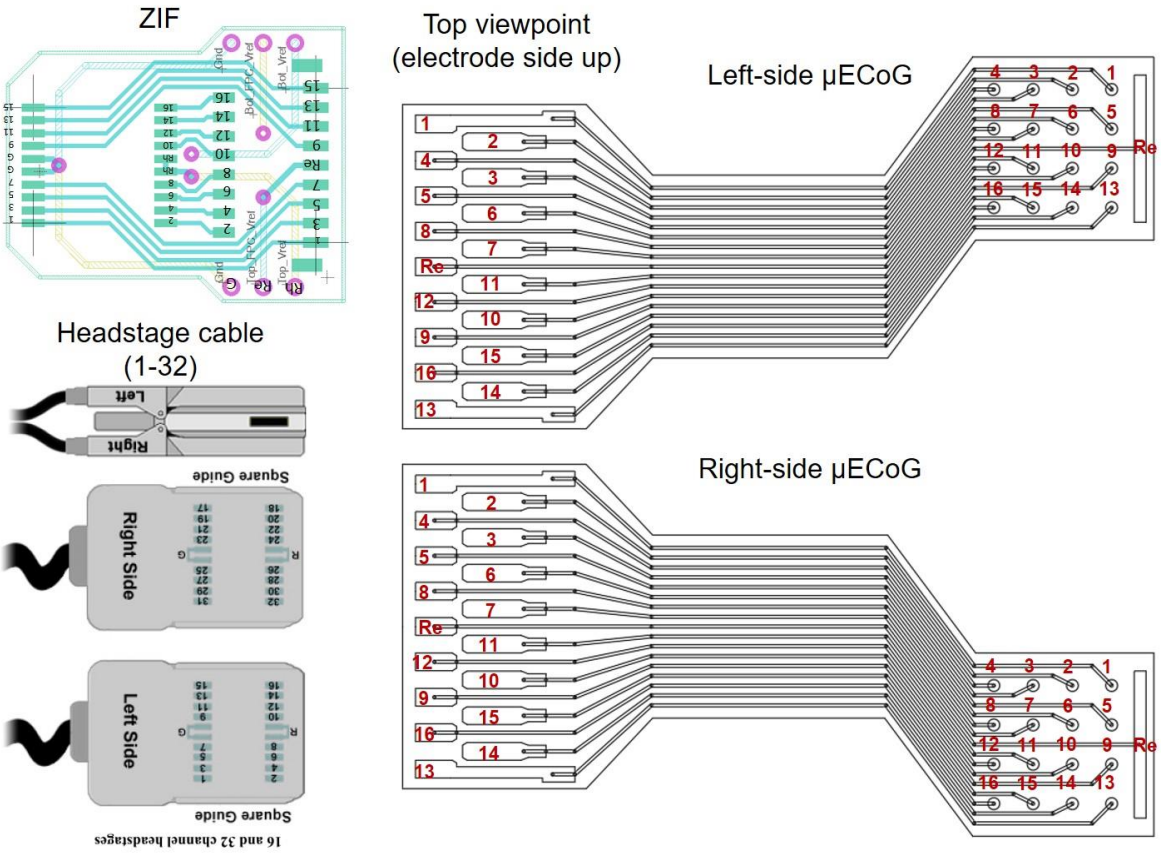

Figure B.1. Electrode maps of the integrated μECoG device. Left-side and right-side devices are connected 1-32 headstage channel cable between ZIF connector and the recording equipment for measuring a neural and electrical signal.

Appendix C. Photograph images of the cranial prothesis

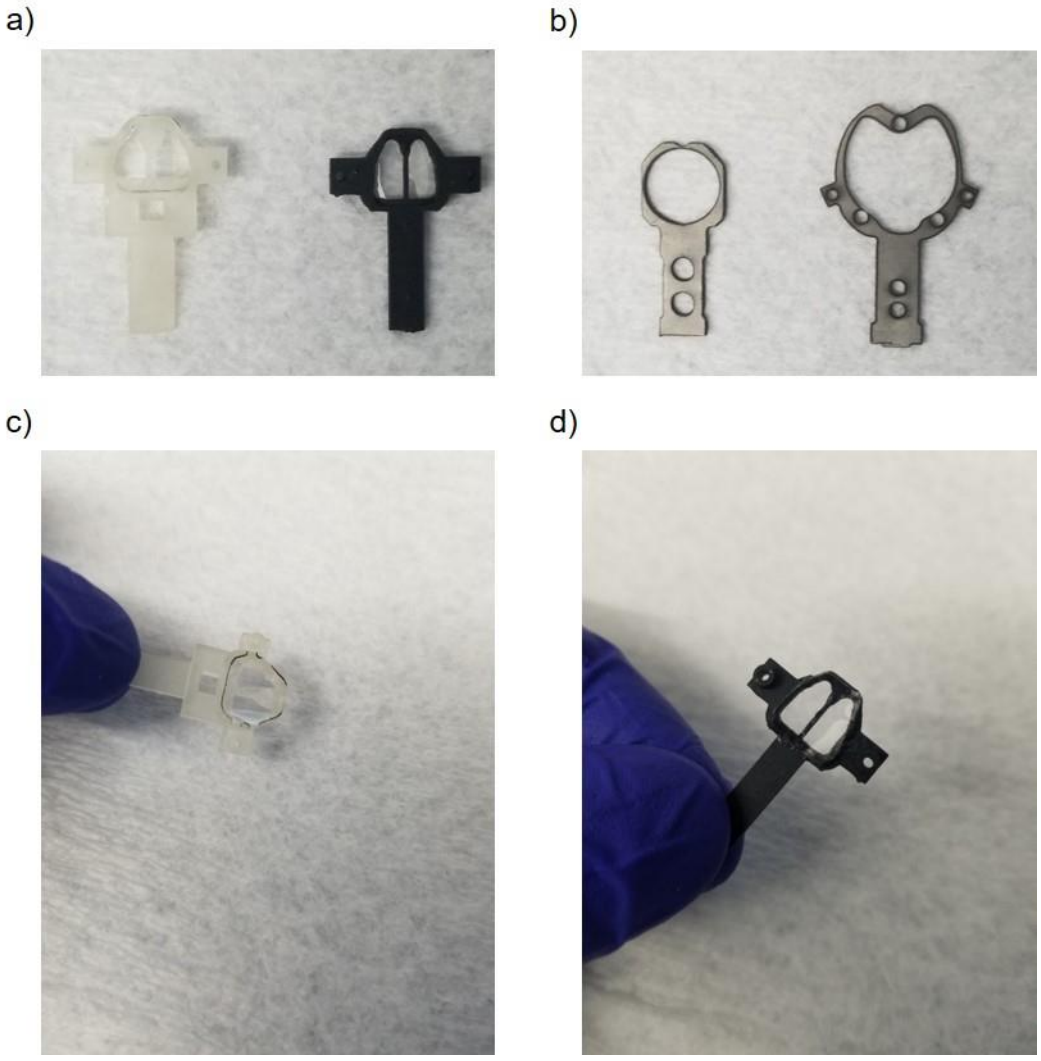

Figure C.1. Photograph images for the cranial prothesis by 3D-printed polymethylmethacrylate (PMMA) and Titanium (Ti). a) A frame for the attachment of the μECoG device with boned flexible polyethylene terephthalate (PET) film. b) Titanium head-plate to support the stable mechanical property. c-d) side view of optical images both 3D-prined PMMA frame (white and black) with flexible PET film. The Titanium head-plate and 3D-printed PMMA frame are assembled in the final stage [77].